NAVAL
POSTGRADUATE
SCHOOL

MONTEREY, CALIFORNIA

THESIS

ADDITIVE MANUFACTURING OF ALUMINUM ALLOY COMPONENTS SUITABLE FOR MARINE APPLICATION

by

Zhixian Gerald Qiu

June 2021

Thesis Advisor:	Ibrahim E. Gunduz
Second Reader:	Walter Smith

Approved for public release. Distribution is unlimited.

THIS PAGE INTENTIONALLY LEFT BLANK

REPORT DOCUMENTATION PAGE	*Form Approved OMB No. 0704-0188*

Public reporting burden for this collection of information is estimated to average 1 hour per response, including the time for reviewing instruction, searching existing data sources, gathering and maintaining the data needed, and completing and reviewing the collection of information. Send comments regarding this burden estimate or any other aspect of this collection of information, including suggestions for reducing this burden, to Washington headquarters Services, Directorate for Information Operations and Reports, 1215 Jefferson Davis Highway, Suite 1204, Arlington, VA 22202-4302, and to the Office of Management and Budget, Paperwork Reduction Project (0704-0188) Washington, DC, 20503.

1. AGENCY USE ONLY *(Leave blank)*	2. REPORT DATE June 2021	3. REPORT TYPE AND DATES COVERED Master's thesis

4. TITLE AND SUBTITLE ADDITIVE MANUFACTURING OF ALUMINUM ALLOY COMPONENTS SUITABLE FOR MARINE APPLICATION		5. FUNDING NUMBERS
6. AUTHOR(S) Zhixian Gerald Qiu		

7. PERFORMING ORGANIZATION NAME(S) AND ADDRESS(ES) Naval Postgraduate School Monterey, CA 93943-5000	8. PERFORMING ORGANIZATION REPORT NUMBER

9. SPONSORING / MONITORING AGENCY NAME(S) AND ADDRESS(ES) N/A	10. SPONSORING / MONITORING AGENCY REPORT NUMBER

11. SUPPLEMENTARY NOTES The views expressed in this thesis are those of the author and do not reflect the official policy or position of the Department of Defense or the U.S. Government.

12a. DISTRIBUTION / AVAILABILITY STATEMENT Approved for public release. Distribution is unlimited.	12b. DISTRIBUTION CODE A

13. ABSTRACT (maximum 200 words)

Additive manufacturing (AM) enables precise control of part shapes and can build geometries that cannot be conventionally produced. AM applications for the Navy include "print on demand" unmanned vessels or impact absorbers for hull protection. The objective of this thesis is to investigate metal AM for the fabrication of low-density water-tight buoyant objects and lightweight energy-absorbing structures to control failure modes. To achieve the objective, a liquid metal printer (Xerox ElemX) was used to print aluminum alloy parts. The CAD design of the buoyant object and energy-absorbing structures was to test the printer's ability to build cavities with overhang geometries. For each of the printed parts, observations of print quality were documented to validate the printer's capabilities and make recommendations to improve the subsequent print jobs. Supported by numerical analysis, key insights into the printer's capabilities were gleaned and documented. The compressive test results for the energy-absorbing structures (void infill specimen) yielded a higher specific energy dissipation due to its lighter weight and well-structured internal voids. As a simple proof of concept to tailor failure modes, the strategic placement of the internal voids had also resulted in the intended max deformation to occur at the center of the specimen.

14. SUBJECT TERMS Xerox ElemX, liquid metal 3D printer, 3D printer, low-density water-tight buoyant structures, lightweight energy-absorbing structures, determine material properties of the 3D printed part	15. NUMBER OF PAGES 83
	16. PRICE CODE

17. SECURITY CLASSIFICATION OF REPORT Unclassified	18. SECURITY CLASSIFICATION OF THIS PAGE Unclassified	19. SECURITY CLASSIFICATION OF ABSTRACT Unclassified	20. LIMITATION OF ABSTRACT UU

NSN 7540-01-280-5500

Standard Form 298 (Rev. 2-89)
Prescribed by ANSI Std. 239-18

i

THIS PAGE INTENTIONALLY LEFT BLANK

ADDITIVE MANUFACTURING OF ALUMINUM ALLOY COMPONENTS
SUITABLE FOR MARINE APPLICATION

Zhixian Gerald Qiu
Major, Republic of Singapore Navy
BME, National University of Singapore, 2008

Submitted in partial fulfillment of the
requirements for the degree of

MASTER OF SCIENCE IN MECHANICAL ENGINEERING

from the

**NAVAL POSTGRADUATE SCHOOL
June 2021**

Approved by: Ibrahim E. Gunduz
              Advisor

              Walter Smith
              Second Reader

              Garth V. Hobson
              Chair, Department of Mechanical and Aerospace Engineering

iii

THIS PAGE INTENTIONALLY LEFT BLANK

ABSTRACT

Additive manufacturing (AM) enables precise control of part shapes and can build geometries that cannot be conventionally produced. AM applications for the Navy include "print on demand" unmanned vessels or impact absorbers for hull protection. The objective of this thesis is to investigate metal AM for the fabrication of low-density water-tight buoyant objects and lightweight energy-absorbing structures to control failure modes. To achieve the objective, a liquid metal printer (Xerox ElemX) was used to print aluminum alloy parts. The CAD design of the buoyant object and energy-absorbing structures was to test the printer's ability to build cavities with overhang geometries. For each of the printed parts, observations of print quality were documented to validate the printer's capabilities and make recommendations to improve the subsequent print jobs. Supported by numerical analysis, key insights into the printer's capabilities were gleaned and documented. The compressive test results for the energy-absorbing structures (void infill specimen) yielded a higher specific energy dissipation due to its lighter weight and well-structured internal voids. As a simple proof of concept to tailor failure modes, the strategic placement of the internal voids had also resulted in the intended max deformation to occur at the center of the specimen.

THIS PAGE INTENTIONALLY LEFT BLANK

TABLE OF CONTENTS

LIST OF FIGURES

x

THIS PAGE INTENTIONALLY LEFT BLANK

LIST OF TABLES

THIS PAGE INTENTIONALLY LEFT BLANK

ACKNOWLEDGMENTS

tight, and I had only one week to operate the machine, for which Dr. Park kindly accommodated my time slot.

Finally, I would like to thank my wife and family for the physical and mental support they gave me to complete this research. With their unwavering support back in Singapore, I focused entirely on the task at hand while conducting meaningful research and fulfilling the required thesis objectives.

I.   INTRODUCTION

A.   MOTIVATION

Global Marine Trends. The environment in which navies operate will be increasingly volatile, complex and congested. Primarily driven by the opening of the economies of the developing countries, the increase in consumerism and energy demands directly increase the amount of tonnage and goods transported via the sea. These will profoundly impact commercial shipping requirements and natural resource exploitation; "an emerging shift of geopolitical configurations where future competitions and conflicts between nations are more likely to involve future competition at sea" [1]. Maritime states or nations whose livelihood depends on the sea may see an increase in unconventional threats such as piracy, conflicts out at sea due to congested waters, and contestation of the exclusive economic zone.

Unconventional Warfare. Today's navies have to deal with unconventional warfare such as piracy, asymmetrical warfare, contestation at sea and maritime terrorism. For example, in a maritime state such as Singapore, it is vital that the sea lanes of communication remain open for trade and economic progress. Therefore, any disruptions to the sea lanes or piracy may affect the stability of the country. There has been a surge in piracy activities in recent years, and especially in 2020, more piracy cases have been reported in the Straits of Singapore than in the whole of 2019 [2]. The total incidents reported in 2020 were 33, surpassing the 31 incidents reported in 2019 [2]. In response to the maritime piracy incidents, Singapore refurbished the decommissioned patrol vessels and quickly inducted non-lethal options and capabilities to deal with maritime incidents [3]. The above situation is an example of the volatile and complex maritime domain that the coastal navies are grappling with, not traditional warfare but of an unconventional situation such as piracy. This will require any navy to be adaptable and agile in its capability's induction program and leverage technologies to improve maritime situational awareness, data collection and support lean manning for the wide span of operations.

Paradigm Shift in Naval Fighting Concepts. Naval platforms of the past were developed for conventional threats and security issues. However, with emerging disruptive technologies and the evolving trends of the maritime domain, coupled with limited resources and manpower constraints, there is a paradigm shift in the way navies operate and structure. Assets will need to be multi-role and adaptable to quickly meet the broad spectrum of operations in dealing with arising maritime security issues, humanitarian aid, and disaster relief. Navies will need to leverage disruptive technologies to develop countermeasures against low-cost assembled threats and support the whole range of maritime operations in a sustainable manner through lean manning while ensuring the human is placed out of harm's way. As articulated by the U.S. Navy Chief of naval operations in the navy's strategy guidance issued via a fragmentary order (FRAGO), "The future navy will need to incorporate manned and unmanned teaming and autonomy to address the increasingly congested and contested operating environments. Thus, to make the fleet more survivable and resilient, the U.S. Navy will need to leverage technology to expand their reach, lethality and warfighter awareness" [4].

Light-Weighting Fundamentals. To ensure that the fleet continues to be survivable and resilient, the U.S. military has constantly been balancing the need for performance, protection and payload while maintaining affordability. Therefore, light-weighting concepts seek to reduce cost without compromising on performance and protection. With lightweight constructions, naval vessels will improve range, fuel efficiencies, payload capacities while being afforded the required protection (i.e., high specific energy absorption capacities). However, to incorporate the design of lightweight material into a vessel's construction (hull, mast, secondary structures) and realize the benefits requires the knowledge of the material in terms of the possible design strategies and the fabrication techniques associated with it [5].

Advancement in Manufacturing Methods. To enable the fleet to be agile and adaptive, advanced manufacturing solutions such as the exploitation of 3D printing will enable the fleet to shift their "logistics base" to the front line and streamline the entire logistics supply chain to support on-demand requirements. Emerging 3D printers such as the ElemX liquid metal 3D printer support quick fabrication that traditional manufacturing

methods will not achieve. Thus, enabling the navies to test conceptual fighting models and shorten the time required to develop new capabilities required for specific mission sets. The "Global marine technology trends 2030" report recommends investing in print-on-demand unmanned vessels which can work with manned vessels. It involves 3D printing "disposable ships" or readily configured unmanned vessels (underwater, surface, air) to meet mission requirements [1]. The Royal Navy had begun 3D printing customized drones on board the ships to meet specific mission requirements. Thus, it will enhance its flexibility to carry out different mission sets such as surveillance, mine-hunting, and humanitarian assistance, improving its ability to attain mission success [6].

Furthermore, with the advancement of 3D printing technology, it is now possible to fabricate complex internal geometries. Moreover, because 3D printing builds layer upon layer, it also demonstrated the ability to precisely control the part development of intricate internal cell structures or cavities. This opened numerous possibilities in developing lightweight and possibly buoyant structures with high stiffness and energy absorption capacities suitable for marine applications.

B. BACKGROUND

As a proof of concept to showcase the capabilities of the Xerox ElemX liquid metal 3D printer against traditional manufacturing methods, this research work shall explore the usage of an aluminum A356 (4008) casting alloy as the main metal filament to conduct additive manufacturing (AM) of simple objects such as; (1) Low-density water-tight buoyant structures designed for flotation, and (2) Lightweight energy-absorbing structures with controllable failure modes for naval applications. This research will also conduct numerical analysis to determine the effects of ambient and print bed temperature on the cooling rate of the metal droplet, and consequentially the microstructure of the 3D printed part.

1. Additive Manufacturing (AM)

The development of AM methods enables many possibilities in part design and composition afforded by the creation of a 3D object layer by layer. In today's context, 3D printing has moved from prototyping to customization and even large-scale production,

potentially disrupting traditional methods of component production such as CNC machining, injection molding, and casting. The number of AM methods have also increased during the last 30 odd years; currently, there are seven major methods (refer to **Figure 1**); namely, (1) Vat Photo-Polymerization, (2) Material Jetting, (3) Material Extrusion, (4) Binder Jetting, (5) Powder Bed Fusion, (6) Sheet Lamination and (7) Directed Energy Deposition to 3D-print parts either indirectly or directly depending on the application, material type and geometry requirements [7].
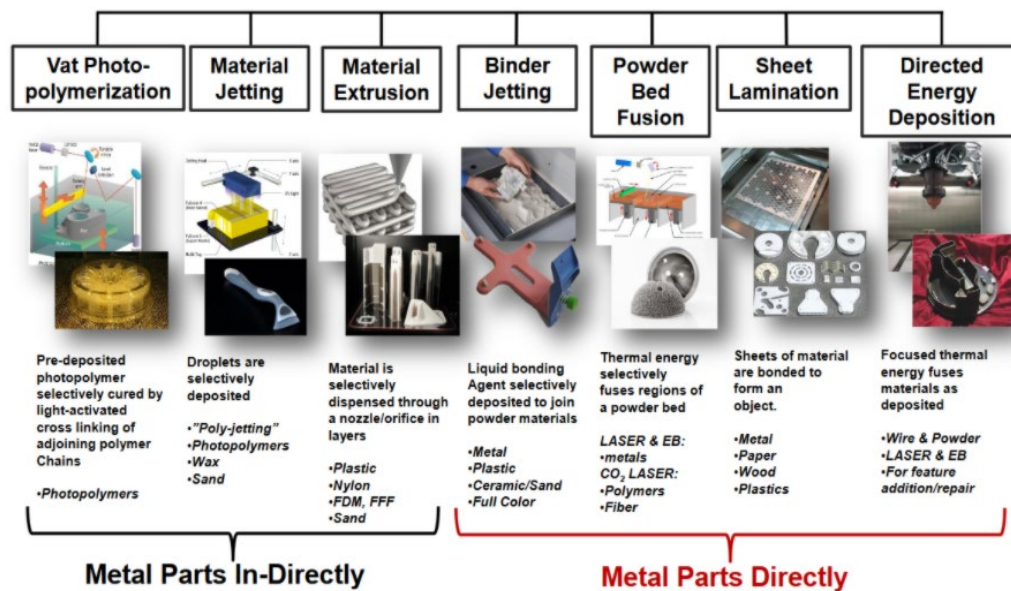
Figure 1.   Seven additive manufacturing processes according to ASTM committee F42 on additive manufacturing. Source: [7].

In general, AM refers to depositing thin layers or droplets of material layer by layer (on top of one another) to produce a 3D object. Based on Statista, "The most used 3D printing technologies in 2020" is (1) Fused Deposition Modeling (FDM) followed by (2) Selective Laser Melting (SLM) [8]. The FDM—otherwise known as fused filament fabrication (FFF) or material extrusion, works by melting the thermoplastic filament (polymer or metal composite) and depositing it layer by layer through the nozzle tip to build the desired object. SLM uses a high-powered laser to fuse/sinter powders of the material to create the desired shape.

As opposed to conventional manufacturing, the advantages and value of AM are that AM has a high degree of customization with the ability to print complex geometries and fabricate internal cavities or voids (in an orderly shaped manner) that traditional manufacturing methods could not achieve. Furthermore, 3D printing has the option to print "the whole part" without the need to separately manufacture and assemble the product. These advantages, coupled with rapid prototyping, is suited for military applications.

There are, however, challenges that come with AM. The build volume of the printers is usually limited, and hence not all marine parts or components can be printed as a whole. In terms of cost-effectiveness, traditional mass-production methods to manufacture a high volume of parts is still cheaper than AM, and the time required to mass-produce 3D printed parts may be much longer than conventional methods. Compounded with this is the lack of standards to govern 3D printed parts, especially for marine applications. For example, marine parts/components will need to be certified by class standards to determine whether it is seaworthy or if it directly affects the safety of the ship. Without endorsement or laying of ground rules from governing/safety bodies, 3D printed parts could only be used for the non-critical systems without fulfilling its fullest potential.

2.   3D-Printed Unmanned Vessels

Following the example of the print-on-demand unmanned drones/vessels envisioned by the Royal Navy, it is now possible to **print an unmanned surface/ underwater vessel with internal structures (voids) that are water-tight to mitigate capsizing** while fitted with the necessary modules to carry out the specific mission type. The unmanned industries have started to demonstrate capabilities and capacities to successfully build and sail 3D printed unmanned vessels. **Figure 2** shows an unmanned vessel developed by Auto Naut that is 3D printed mostly with nylon resin. The stern cone, fins and hull mounts have been 3D printed with the possibility of ruggedization to survive when placed in harsh environments [9]. The unmanned vessel shown in **Figure 3** was also developed by Auto Naut using the laser sintering (SLS) process. The main reason for using this method was that the powder bed could support the part printing without any additional in-build support. The challenging portion was to print the intricate

parts (which accounted for 30% of the boat) of the bow and the unmanned vessel's tail fins and ensure that it is non-porous [10]. **Figure 4** shows the "Nautilus 100 mothership," an unmanned underwater vessel that looks like a manta ray, which was co-developed by the Royal Navy and industrial partners. Its hull is designed to be 3D printed from a combination of light but strong acrylic materials bonded to super-strong alloys, which will help withstand the extreme pressure experienced at the depths of the sea [11].

Figure 2.   Auto Naut 3D printed vessel could capsize and self-right.
Source: [9].

Figure 3.   Auto Naut 3D printed vessel, built by laser sintering method.
Source: [10].
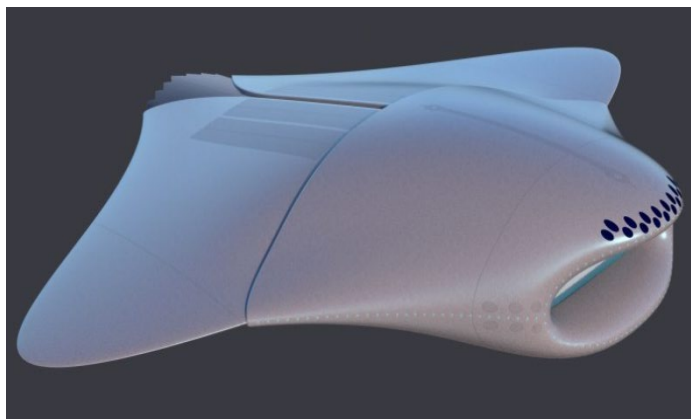
Figure 4.   "Nautilus 100 mothership," developed by Royal Navy.
Source: [11].

3.   Energy Absorbing Structures

Cellular Solids. We can find cellular solids in nature; examples such as wood, sponge and even bone have solid edges and faces interconnected to fill space [12]. In simple terms, a cellular solid is structured to contain internal voids or cavities of different geometries designed to achieve material properties that are suitable for engineering/ structural applications. Cellular solids can have internal pattern ranging from the "honeycomb," "foam," and "lattices" structures, as shown in **Figure 5**. Depending on the capabilities of manufacturing methods, internal structures will consist of either perfectly ordered or disordered cell patterns. Cellular solids are lightweight with excellent specific strength/energy absorption properties and widely used in applications summarized in **Table 1** [13].
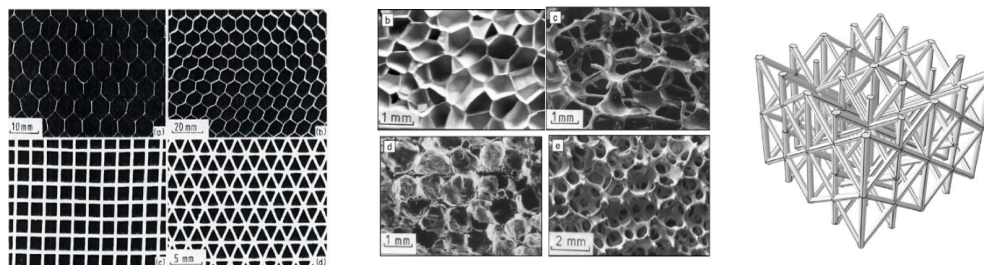
Figure 5.   Honeycomb (left), foam (middle), lattice (right). Source:[12], [13].

Table 1.   Application of cellular structures. Source: [13].

Type of Cellular Structure	Applications
Foams	Energy Absorbers, Filters, Silencers, Flame arrestors, Heaters and Heat exchangers, Electro-Chemical Devices
Honeycomb	Energy Absorbers, Biomedical Implants, Filters, Sensors, Actuators, Vibration absorber or damper
Lattices	Energy Absorbers, Heaters and Heat Exchangers, Engine Hood, Biomedical implants, Wings, Gas turbine engine fan blades, Vibration absorber, Robotic System, Spacecraft and aircraft structures (fuselage)

Cell Structure and Shape. The cell can be shaped in various geometries and may be stacked in various arrangements and differing connectivity between the cell interface, resulting in different material properties [12]. The mechanical properties of the component are therefore dependent on the unit cell architecture and the stacking pattern. As a result, several studies focused on the role of cell topology optimization to enhance the mechanical properties of structures. For example, topology optimization combined with numerical homogenization has been used to design materials with tailored mechanical properties [14]. The fundamental cell structure has regular shapes shown in **Figure 6**, while **Figure 7** shows the various possibilities to stack or arrange the cell in a 2D plane. In **Figure 8**, the variety of 3D shaped cells can also be packed together to form lattice structures optimized to achieve the desired material properties.
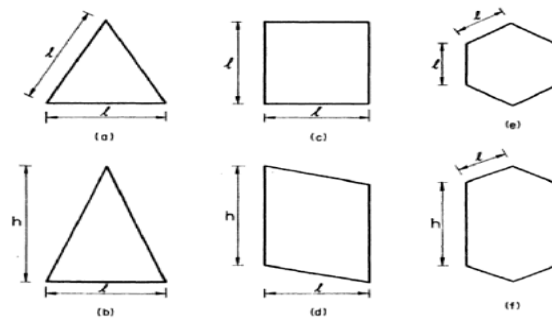
Figure 6.   Polygons of different shapes. Source: [12].
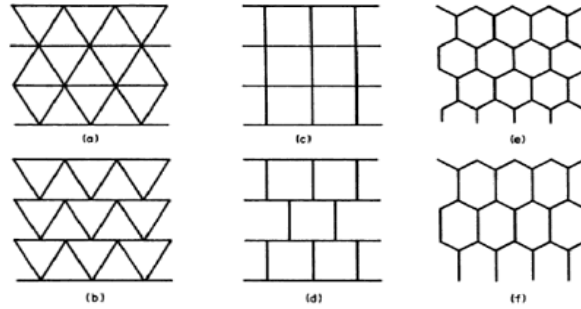
Figure 7.   Packing of two-dimensional cells to fill a plane. Source: [12].
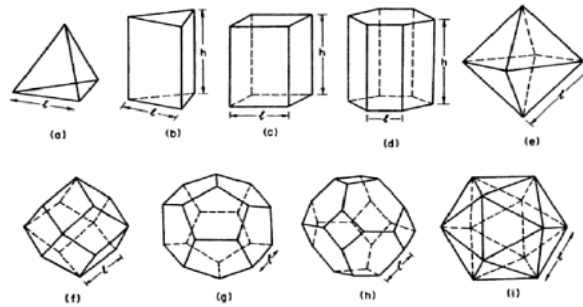
Figure 8.   Three-dimensional polyhedral cells. Source: [12].

Traditional Manufacturing Vs 3D Printing. In traditional manufacturing methods, it is not possible to build enclosed or water-tight structures with internal cavities. Furthermore, there are also limitations to building metal foam parts with internal close/ open cells, i.e., having no control in the positioning and size of the cell cavity. However, with the advancement of 3D printing technology, it is now possible to fabricate complex internal geometries. Moreover, because 3D printing builds layer upon layer, it also demonstrated the ability to precisely control the part development of intricate internal cell structures or cavities; for example, the 3D printed internal cavities, as shown in **Figure 9a,** illustrates the open cellular structure [15]. **Figure 9b** shows the internal void hollowing (rhombus shaped) while maintaining the external appearance of the object [16]. On the other hand, closed-cell metal foams developed by traditional manufacturing methods involve injecting inert gas bubbles into the molten metal to randomly place and create cells within the metal, resulting in uncontrolled porosity and density (**Figure 9c**).

9
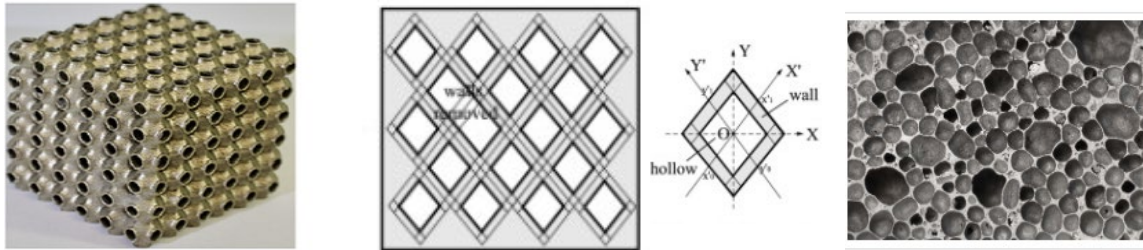
Sheet - Primitive

a) 3D printed primitive
shaped open cell [15]

b) 3D printed rhombus
shaped voids [16]

c) Closed cells manufactured
by traditional methods [17]

Figure 9.   3D printing versus traditional manufactured parts. Source: [15],
[16], [17].

Marine Application. The selected material for this thesis is aluminum due to its low density, excellent durability and corrosion-resistant properties. Thus, fully enclosed water-tight cellular solids made of corrosion-resistant aluminum has potential application for the marine and shipbuilding industries. The cellular metal structure has a high strength to weight ratio, making it suitable for ship structures (hatches, mast, hull). Because it is water-tight, it will also be suitable for buoyancy-related applications.

Furthermore, metal cellular structures (foams, lattices, honeycombs) can absorb energy because of their internal structure and porosity. Lightweight aluminum foam, for example, can absorb a large quantity of mechanical energy during deformation [18] and even when stresses exceed the compressive yield strength. Enclosed metal shells/panels with an internal sandwich, lattices or honeycomb structures of different cell geometries/ shapes have also been studied to improve the load-bearing and energy absorbing capacities. To this end, optimizing the gradient design of the cell structure (**Figure 10**), for example, will enhance the energy absorption capacities and achieve controllable deformation/failure modes [19]. Therefore, these energy-absorbing structures coupled with controllable failure modes are well suited for marine applications such as (1) Fenders support system to "cushion" ships while berthing or (2) Hull protection to absorb direct kinetic impact from ship collision out at sea.
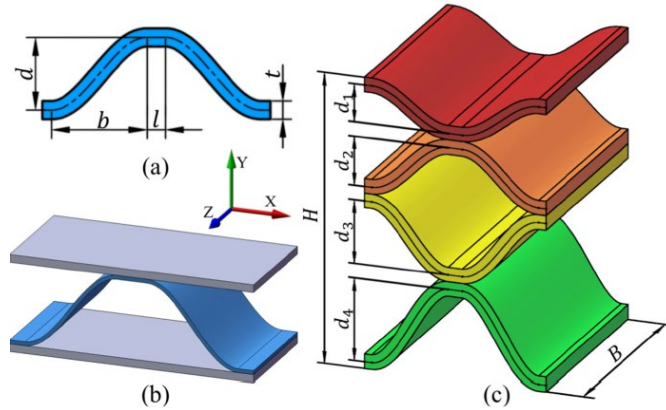
Figure 10.   Gradient design to enhance energy absorption capacity, facilitates
layer-by-layer deformation and reduces load fluctuations. Source: [19].

4.   Xerox ElemX Liquid Metal 3D Printer

The state-of-the-art Xerox Liquid Metal 3D printer (classified under material jetting) will be tested and utilized to create 3D printed marine parts through a patented metal 3D printing technology known as "magnet-o-jet." This technology was slated to produce parts rapidly, minimize material wastage, and save cost by using commercially off the shelf wire feedstock [20]. The system will load a non-specialty metal wire such as the aluminum alloy (4008) into the ElemX machine. The metal wire gets melted in a heated reservoir, filling up the ejection chamber with molten metal. The molten metal then gets directed out of the nozzle in droplet jets induced by external magnetic fields that generate magnetohydrodynamic effects in the melt without direct contact. This process is repeated on each droplet using an electrical pulse up to a rate of 500 times a second, which results in a high deposition rate. The Xerox ElemX, as illustrated in **Figure 11**, can also handle a range of aluminum alloys such as the 6061 and the 7075 [20].

11

Figure 11.   Xerox ElemX 3D printer and an example of a printed aluminum
part. Source: [21].

5.   Characterization and Numerical Analysis of Additively Manufactured Products

To better understand the properties of the 3D printed parts, the following will be conducted: (a) Compressive test to evaluate mechanical properties concerning its structure, and (b) Numerical Analysis of the metal droplet cooling rates and temperature profile.

a.   Compressive Testing

Compression tests are required to determine the material's behavior under applied loads. It is conducted by applying a compressive force on a specimen with a cylindrical geometry following the American society for testing and materials (ASTM) standards. The Instron compressive testing machine shall be utilized to determine material properties such as the yield strength, compression modulus, toughness and specific energy absorption of the specimen. **Figure 12** shows the Instron compressive testing machine that will be utilized to conduct the test.

Figure 12.   Instron compressive testing machine. Source: [22].

b.   Numerical Analysis of the Metal Droplet Thermal State

Cooling rates and subsequent solidification of the molten metal droplet will determine the size of the dendrites and grains that ultimately affects the mechanical properties of the material. The faster the cooling rate, the finer the grain size, therefore producing materials with higher strength. The effects of ambient and print bed/substrate temperature will be analyzed in this work to determine if there are significant influence on the thermal state of the metal droplet.

(1)   Ambient Temperature effects on the thermal state of the Metal Droplet. Upon ejection of the metal droplet from the print head, the droplet will be exposed to the surrounding ambient temperature during flight. The lumped capacitance method and exact solutions (include spatial effects) for transient heat conduction will be utilized to determine the temperature profile of the droplet during flight.

(2)   Print bed/Substrate Temperature effects on the thermal state of the "Planar Splat." Once the droplet collides with the print bed (or aluminum substrate), the droplet will form a "planar splat." Heat dissipation through natural convection and radiation is considered negligible due to the short time span. The temperature profile of the "planar splat" will be determine through the heat conduction and energy conservation equations.

C.   OBJECTIVES

Traditional manufacturing methods such as casting or metal injection molding cannot build a part that has internal cavities with specific geometries or prescribed shapes. Thus, this thesis shall explore the usage of aluminum alloy (4008) as the main metal filament to conduct additive manufacturing of simple objects to **showcase the capabilities and feasibility of the Xerox ElemX liquid metal 3D printer against traditional manufacturing methods**.

Objective #1. Through 3D printing, this research intends to demonstrate the 3D printer's capability to **build low density water-tight buoyant structures with internal cavities** designed for floatation and to **validate the possibilities of printing a hull-shaped water-tight object** (mimic hull of an unmanned vessel). The following objects shall be printed and proof of concept to see if it floats and maintains the water-tight integrity.

      a.   **X-shaped object with square voids.**

      b.   **X-shaped object with parallelogram voids.**

      c.   **Double parallelogram-shaped object with parallelogram voids.**

      d.   **Cube-shaped object with repeated square voids.**

Objective #2. Through 3D printing, this research intends to test and demonstrate the 3D printer's ability to fabricate lightweight energy-absorbing structures with the intention to control deformation and failure modes. Compressive testing will be conducted to determine the material properties (such as compressive yield strength, elastic limit, and specific energy absorption) of the 3D printed part (cellular solid). The following test specimens shall be printed as proof of concept to fulfil the objectives of the thesis paper.

      a.   **Cylinder with solid infill (25mm height, 13mm diameter).**

      b.   **Cylindrical with void infill (25mm height, 13mm diameter).**

Objective #3. Through numerical analysis, investigate the effects of the ambient and print bed/substrate temperature on the thermal state of the metal droplet. Draw a correlation between the ambient and print bed/substrate temperature with the temperature profile of the metal droplet/splat.

     a.   **Ambient temperature effects on the thermal state of the metal droplet.**

     b.   **Print bed and substrate temperature effects on the thermal state of the "planar splat."**

THIS PAGE INTENTIONALLY LEFT BLANK

II. EXPERIMENTAL METHODS

A. PREPARATION FOR 3D PRINTING

1. Operational Procedures for the Xerox ElemX 3D Printer [23]

Xerox has developed a **procedural instruction for Version 1.0** of the software and hardware setup to guide the user to operate and troubleshoot the 3D printer [23]. This ensures that the 3D printer meets performance specifications, such that the liquid metal jetting, surface finish, and deposition are of the highest quality. The operational procedures consist of the following phases: (1) **Pre-Start Checks**, (2) **3D Printer Start-up**, (3) **3D Printer Calibration**, (4) **Execute Print-Job**, (5) **3D Printer Re-calibration** and (6) **3D Printer Shut down**.

2. 3D Printer Design Guidelines and Machine Specification [24]

The 3D printer is currently undergoing trial and review; therefore, the printer's guidelines such as build volume and weight specification, for example, are spec conservatively. With future software and hardware modification/upgrades, the guidelines will also change accordingly. These guidelines are important design inputs that the user must consider that will determine the quality and success of the 3D printed part.

3. Design and Modelling of Buoyant Structures

<u>Design of Structure and Internal Cavity</u>. To fabricate low density water-tight buoyant structures with internal cavities, it is necessary to incorporate the printer's design considerations to maximize the probability of a well-printed part. After each model is printed, print errors will be noted and adjustments made (model design, machine calibration etc.) to improve the print quality progressively. Thus, a series of objects were modelled to test the printer's capabilities and to achieve the best outcome possible. The following models were designed using the CAD software "Solid Edge" and to improve the surface resolution of the printed product; Meshmixer refined the CAD model to increase the mesh density and resolution of the model. The basic unit cells (internal cavities) modelled were shaped after a **square** and **parallelogram**.

a. X-Shaped Object with Square Voids

A **square void** was modelled and positioned such that the square is **rotated 45°
about the Y-axis** as shown in **Figure 13**) to meet the general guidelines for **overhang
structures**. The scaled-down design of this part was shaped into an "X" to accommodate
the square voids within. There are 15 voids with a minimum wall thickness of 1 mm to the
surface and 2 mm between voids. The wall thickness was deliberately chosen to be 1 mm
to test the printer's ability to print thin wall features. This scaled-down model is non-
buoyant (insufficient displacement) and is meant to test if the printer could achieve the
desired shape and print quality first before printing the buoyant part (actual scale). The
overall dimension of this scaled-down model is 38.2mm (length) by 42mm (width) by
38.2mm (height). Time taken to model: 1-hour ~.
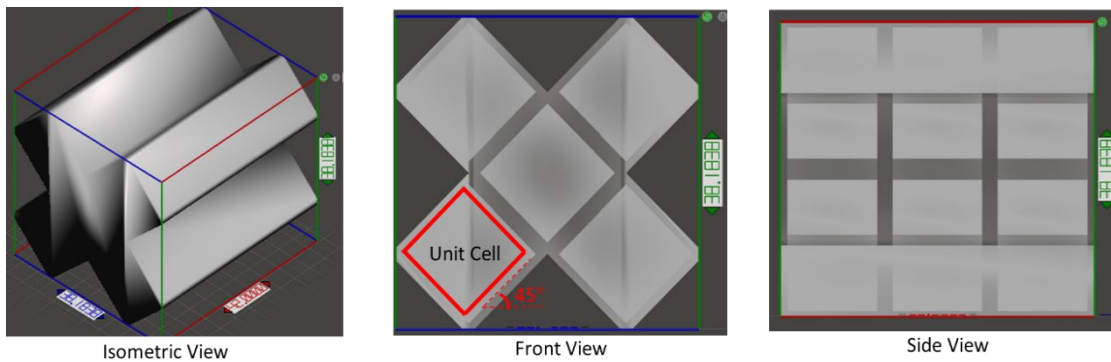
Figure 13.   X-shaped buoyant model (square voids)

b. X-Shaped Object with Parallelogram Voids

A **parallelogram void** was modelled and positioned such that the void is **rotated
60° about the Y-axis** as shown in **Figure 14**. The **parallelogram void was angled at 60°**
to improve the printing feasibility due to its smaller overhang. This is also a scaled-down
design, and it is shaped into a "slim X" to accommodate the parallelogram voids within.
There are a total of 10 voids with a minimum wall thickness of 2mm. The **wall thickness
was adjusted to 2mm** to test if the quality of the printed part would improve. The sharp
edges and corners were also filleted to smoothen the printing process, minimizing sudden

deceleration/acceleration of the print head and improving the accuracy of metal deposition. **Two models were developed for this shape**; (1) **Scaled-down model** measuring 26.8mm (length) by 22.5mm (width) by 35.8mm (height) as shown in **Figure 14**, and (2) **Buoyant model** measuring 76mm (length) by 48.1mm (width) by 77.2mm (height), calculated for sufficient displacement as shown in **Figure 15**. For this to float in water, the density of the actual model is less than 1000kg/m^3. Time taken to model: 1.5 hours~.
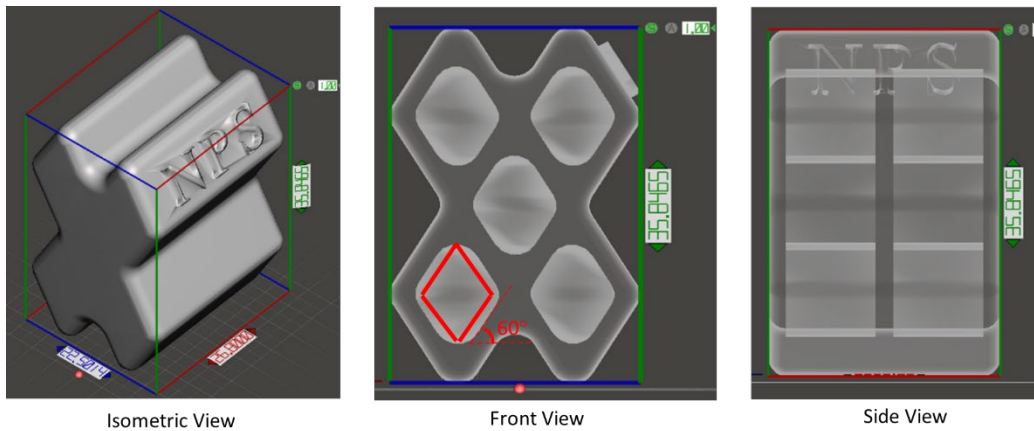
Figure 14. [Scaled-down] X-shaped model (parallelogram voids) with "NPS logo" embossed on the top surface
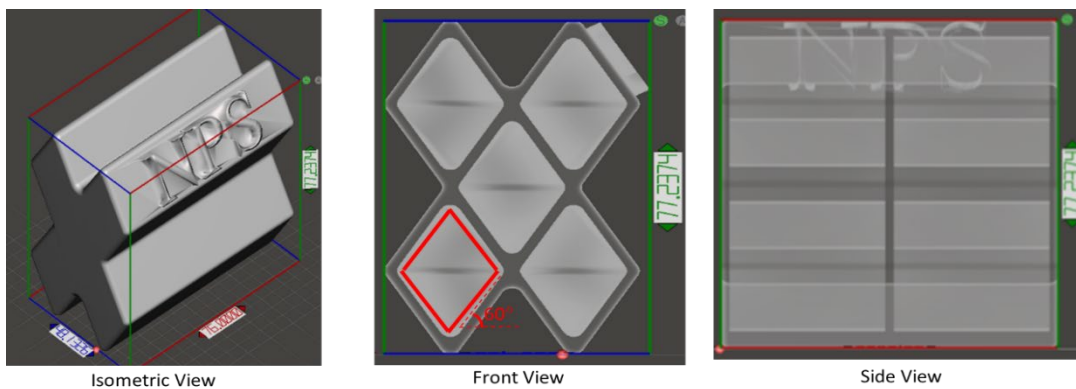
Figure 15. [Actual-scale] X-shaped buoyant model (parallelogram voids) with "NPS logo" embossed on the top surface

c. Double Parallelogram-Shaped Object with Parallelogram Voids

Similar to the previous model, a **parallelogram void** was modelled and **angled at 60°**. A "single-layer" double parallelogram shape was modelled to minimize the build height and accommodate the voids. There are a total of 4 voids with a minimum wall thickness of 2mm. The sharp edges and corners were filleted to smoothen the printing process, minimizing sudden deceleration/acceleration of the print head and improving the accuracy of metal deposition. An actual scale model (buoyant part) was developed for this shape measuring 80mm (length) by 46.2mm (width) by 39.6mm (height), calculated for sufficient displacement as shown in **Figure 16**. Time taken to model: 1-hour ~.

Isometric View   Front View   Side View
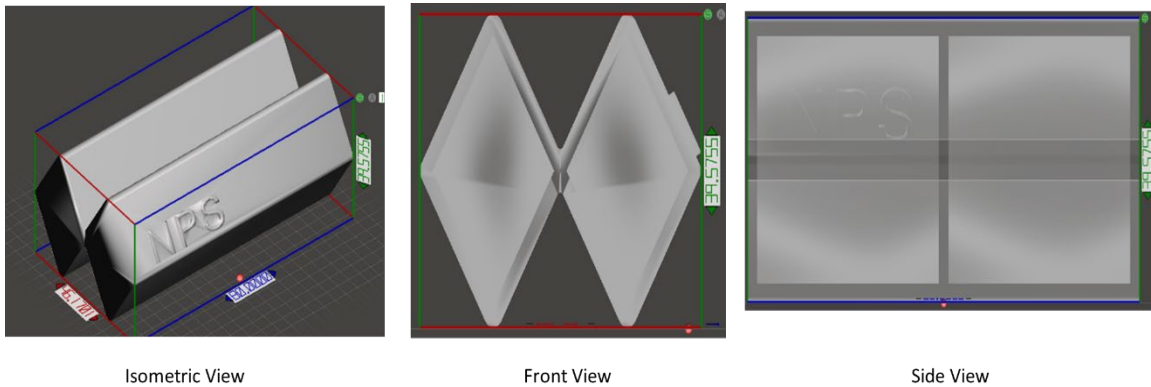
Figure 16.   [Actual-scale] Double parallelogram model with "NPS logo"
embossed on the top surface

d. Cube-Shaped Model with Complex Internal Voids

A **square void** was modelled and positioned such that it is **rotated 45° on both the X/Y axis** as shown in **Figure 17**. The square voids "standing on its tips" are repeated throughout the cube-shaped model. This model's complex geometry is a scaled-down design to mimic repeated void infills such as those found in lattice/sandwich structures. The voids have a minimum wall thickness of 3 mm. The overall dimension of this scaled-down model is 56mm (length) by 56mm (width) by 50mm (height). Time taken to model: 1.5 hours~.

Isometric View   Internal Cell Arrangement (Top View)   Single Void Cell (Square standing on its tip)
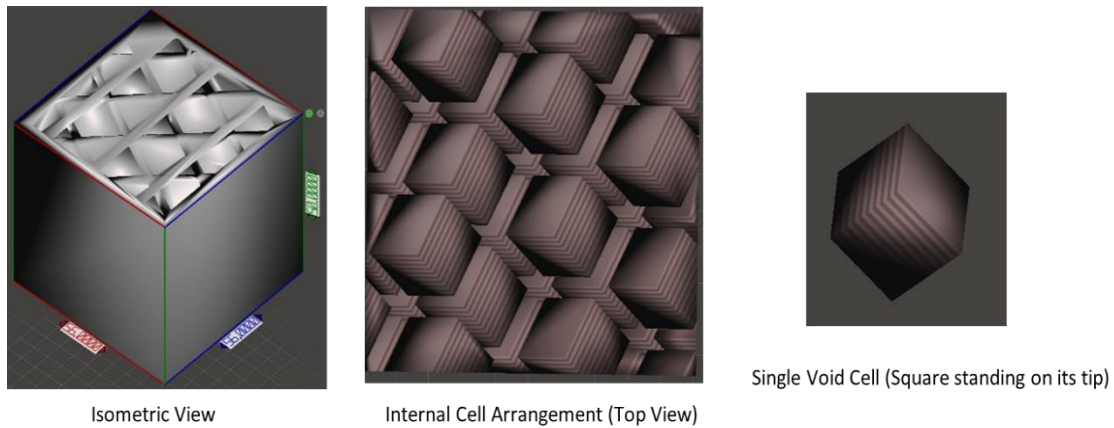
Figure 17. Square cube model with repeated void infill

4. Design and Modelling of Energy-Absorbing Structures

ASTM E9. The ASTM E9 standards for compression testing of metallic materials at room temperature recommended, where feasible, to produce test specimens in solid cylindrical form. To determine the compressive strength and the energy absorption capacities of the test specimen, a **short specimen with an L/D (length/diameter) ratio of two** is selected as it is the best adapted to test this requirement. Referring to **Table 2**, the suggested dimensions for the short solid cylindrical specimens with an L/D ratio of 2 is **13mm by 25mm** (in SI units) [25].

Table 2. Suggested solid cylindrical specimens. Source: [25].

NOTE 1—Metric units represent converted specimen dimensions close to, but not the exact conversion from inch-pound units.

Speci-mens	Diameter		Length		Approx L/D Ratio
	in.	mm	in.	mm	
Short	1.12 ± 0.01	30.0 ± 0.2	1.00 ± 0.05	25.± 1.	0.8
	0.50 ± 0.01	13.0 ± 0.2	1.00 ± 0.05	25. ± 1.	2.0
Medium	0.50 ± 0.01	13.0 ± 0.2	1.50 ± 0.05	38. ± 1.	3.0
	0.80 ± 0.01	20.0 ± 0.2	2.38 ± 0.12	60. ± 3.	3.0
	1.00 ± 0.01	25.0 ± 0.2	3.00 ± 0.12	75. ± 3.	3.0
	1.12 ± 0.01	30.0 ± 0.2	3.38 ± 0.12	85. ± 3.	3.0
Long	0.80 ± 0.01	20.0 ± 0.2	6.38 ± 0.12	160. ± 3.	8.0
	1.25 ± 0.01	32.0 ± 0.2	12.50 min	320 min	10.0

[A] Other length-to-diameter ratios may be used when the test is for compressive yield strength.

Design of Unit Cell. In order to fulfil the requirements of the test objectives, the design and CAD modelling of (1) Solid Cylindrical Specimen (with solid infill) and (2) Solid Cylindrical Specimen (with void infill) was conceptualized by the CAD program- Solid Edge. Moreover, to improve the surface resolution of the printed product, the CAD model was refined by Meshmixer to increase the mesh density and resolution of the model.

a.   Solid Cylindrical Specimen (with solid infill)

This specimen with a dimension of 13mm (diameter) by 25mm (height) was designed and printed with solid infill to serve as the control for the experiment. Data for this control specimen will be collected and compared with the other test specimens. **Figure 18** illustrates the CAD model generated by Solid Edge and refined in Meshmixer.
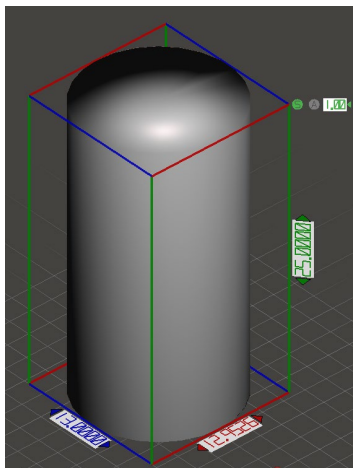
Figure 18.   Cylindrical specimen (solid infill), 13mm (diameter) by 25mm (height)

b.   Solid Cylindrical Specimen (with void infill)

This specimen with a dimension of 13mm (diameter) by 25mm (height) was designed and printed with void infill to determine the performance of the test specimen in relation to the solid infill. The unit cell selected for the void infill is shaped after a 3D cone (**Figure 19a**) stacked together at the base to form a square with 45 degrees overhang when seen on a 2D plane (**Figure 19b**). Internal to the test specimens, the voids are of the same

shape but different dimensions with the intention to control the extent and location of deformation. The "small cone" measured 2.12mm (side) by 3mm (base), and the "big cone" measured 4.95mm (side) by 7mm (base), as shown in **Figure 19c**. The space between voids and wall thickness is 3mm. The positioning of the "big cone" in the center is with the expectation that the maximum deformation is controlled and channeled to occur in the center of the specimen and lesser on the other parts during the compression test.
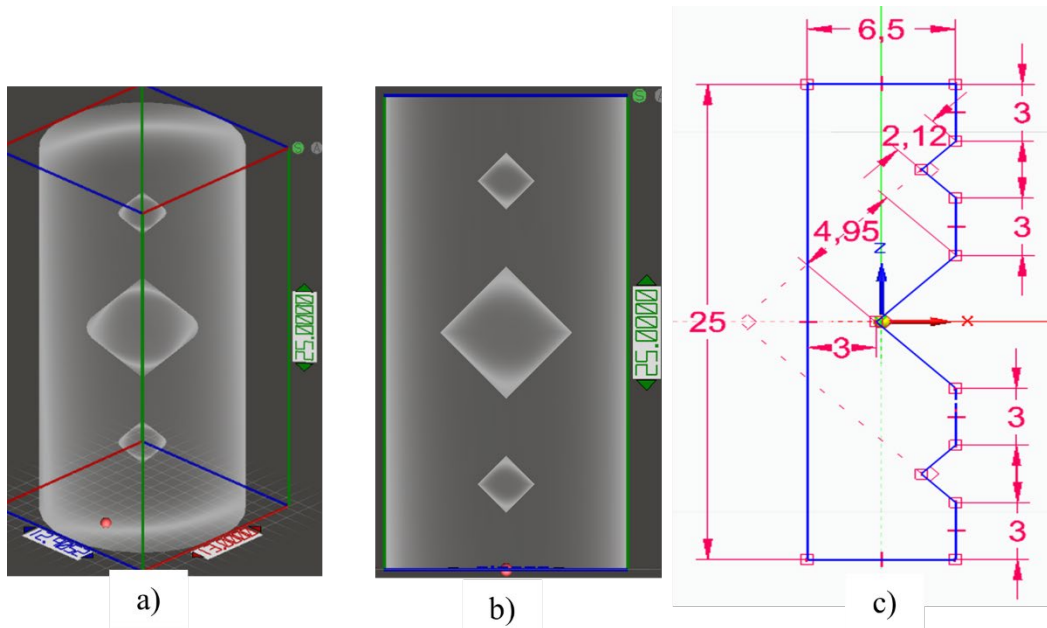
Figure 19.   Cylindrical specimen (void infill), 13mm (diameter) by 25mm (height), with cone-shaped unit cell. 19c shows half the specimen that is revolved around an axis to model the full cylinder

5.   Testing of Energy Absorbing Structures

The Instron compression test machine will be utilized to determine the properties of the 3D printed energy absorbing structures; Cylindrical Specimen (Solid infill and Void infill). During the compression testing, the force-displacement data points are recorded and converted to the stress-strain curve, used to determine mechanical properties such as the elastic limit, yield point, yield strength, compressive strength, and toughness of the material. The test machine used was preset to move at a rate of 20 mm/minute, with a

maximum compressive force of 70 kN. A safety "catch" was also set up to prevent the machine from going beyond the intended displacement.

The printed cylindrical specimen was marked with a simple grid to highlight the deformation shape and grease was applied to the top and bottom surfaces of the specimen to prevent it from getting "stuck" in the set-up, which may lead to undesired buckling. (Refer to **Figure 20**)
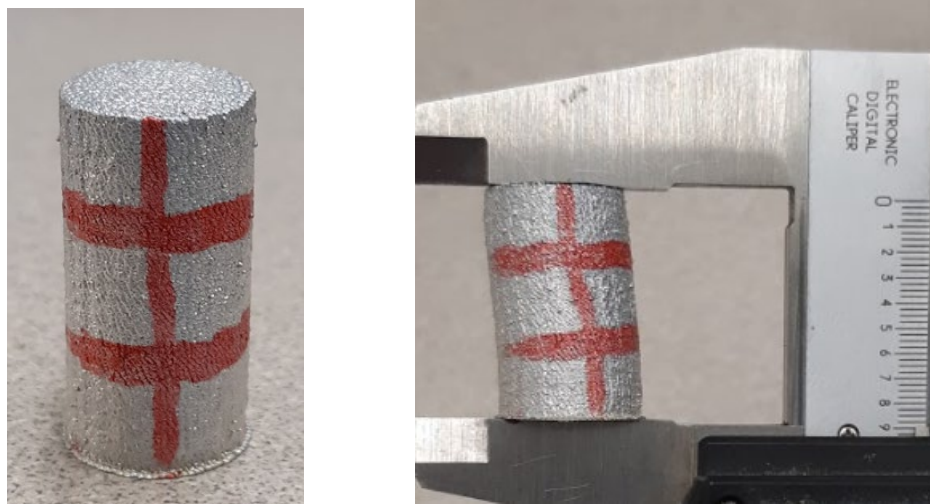
Figure 20.   "Grid" markings on the specimen (left), buckling of specimen (right)

Compressive testing is useful to determine the load-bearing capacity of a support structure and the energy absorption capacities when undergoing compressive stress during its service life [22]. The following parameters were measured during the compression test.

(1)   Yield Strength. Maximum stress the specimen can handle before plastic deformation sets in. It is generally measured by offsetting 0.2% strain and plotting a straight line with the same gradient as the Young's modulus. The intersection point on the curve is the yield strength.

(2)   Compression Modulus. The measure of the material's stiffness and its ability to withstand changes in length when undergoing compressive forces.

This modulus also represents the elastic region, such that if the load is removed, the material returns to its original form.

(3)   <u>Toughness</u>. The material can absorb energy and deform plastically without suffering fracture. The area under the stress-strain curve represents the energy absorbed per unit volume, and it will be measured at 16% strain across all specimens for comparison.

(4)   <u>Specific Energy Absorption</u>. It is defined as the amount of energy that is absorbed by the material per unit mass. This will indicate the performance of the void infill when compared to the solid infill specimen.

THIS PAGE INTENTIONALLY LEFT BLANK

III.   RESULTS AND DISCUSSION

A.   OBJECTIVE 1: BUILD LOW DENSITY WATER-TIGHT BUOYANT STRUCTURES WITH INTERNAL CAVITIES

1.   [Results and Discussion] X-Shaped Object with Square Voids

Printer Setting. This object was printed with **default settings** without global correction or error diffusion. The default setting is akin to carrying out the printing instructions without optimization or receiving feedback from the printed part.

Observations. This printed part took approximately 1.5 hours to complete. The thin walls of 1mm thickness were printed and managed to hold well to form the "X" shape. However, the shape and overhang of the square voids (at the base) were not printed uniformly; this can be observed on the lower tier of the printed part where the overhangs were drooping downwards. This part was printed without correction setting, coupled with accumulative print errors, resulting in the collapse of the square voids at the upper-tier (**Figure 21**). Another observation was the amount of deposited material "falling off" at the specified edge/corner highlighted in **Figure 22**. The print head acceleration and speed through the sharp 90° bend may have contributed to the droplets falling off the edge.
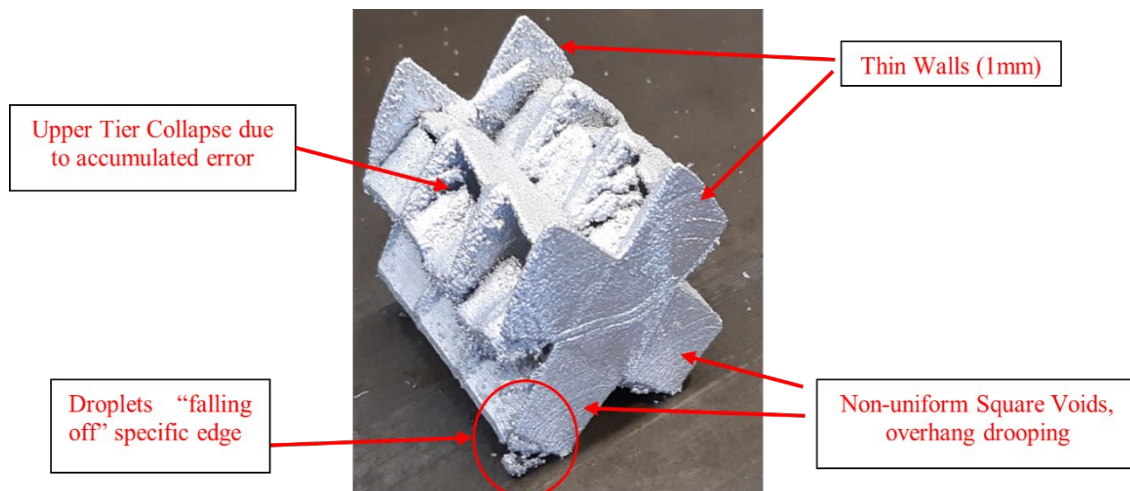
Figure 21.   X-shaped object with square voids (small-scale)
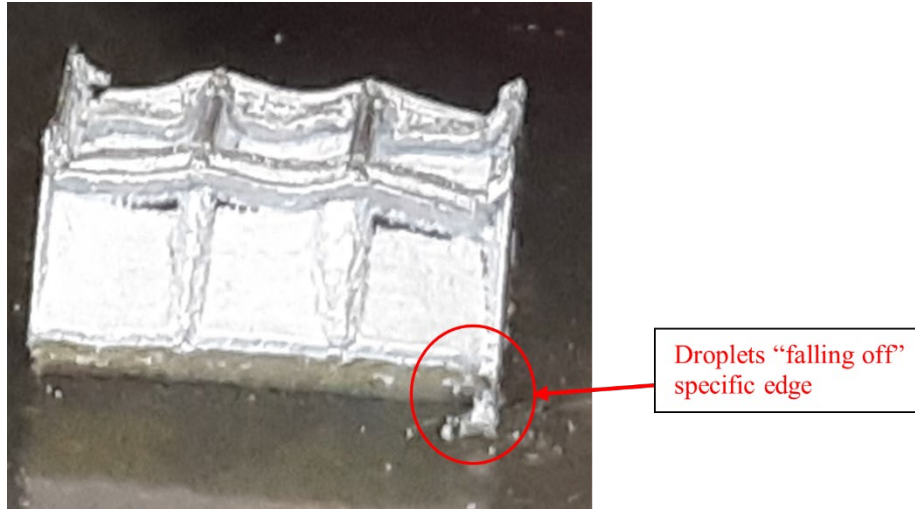
Figure 22.   X-shaped object (printing in progress)

Recommendation. To improve the print quality, the following adjustments were made to the printer's settings as well as to the subsequent models:

a.   **All sharp edges were filleted and rounded to prevent the printer head from taking a sharp turn while turning corners. A rounded corner will facilitate a smoother transition from the X to Y-axis and vice versa. The rounded corners shall be tested with a maximum of 3 mm radius.**

b.   **The overhangs should be adjusted to above 45° to improve the printed void structure's uniformity and prevent it from drooping downwards, leading to subsequent print errors.**

c.   **Wall thickness shall be increased to 2 mm to determine if wall features and overall print quality will improve.**

d.   **Printer settings will be changed to either global correction or error diffusion mode depending on the printer part's dimensions and features.**

2.   [Results and Discussions] X-Shaped Object with Parallelogram Voids

Printer Setting. The **scaled-down model** measuring 26.8mm (length) by 22.5mm (width) by 35.8mm (height) was printed with **global correction (narrow)** since the part is < 3inches in the X-direction. While the **buoyant model measured** 76mm (length) by 48.1mm (width) by 77.2mm (height) was printed with **global correction (wide)** since the part is >3 inches in the X-direction. The algorithm for global correction programs the 3D printer to scan the print part after every five layers to check on the features to determine if compensation is required so that reconfiguration of the droplet spacings and deposition can be adjusted to "average" out the print errors.

Observations for Scaled-Down Model. This printed part took approximately 1.5 hours to complete. The wall thickness of 2 mm and the 60° overhang void structures were printed and managed to hold well to form the "X" shape. However, the shape and overhang of the parallelogram voids (at the base) collapsed slightly at the joint of the lower tier. This is likely due to the rounded fillet (3mm) exceeding the design guidelines, which resulted in the unsupported semi-circle at the tip of the lower tier. Since this part was printed with global correction (narrow scan), the accumulated print errors were "averaged" throughout the print job, which resulted in the gradual slope observed at the tip of the upper tier. This slope is not ideal because it is not according to part specification. It is caused by the compensation and averaging of slight print errors (either over/under mass deposition or sputtering). The embossed letters were too thin to be printed, resulting in the poor-quality finishing on the top side surface. Refer to **Figure 23** for the pictorial description of the printed part.
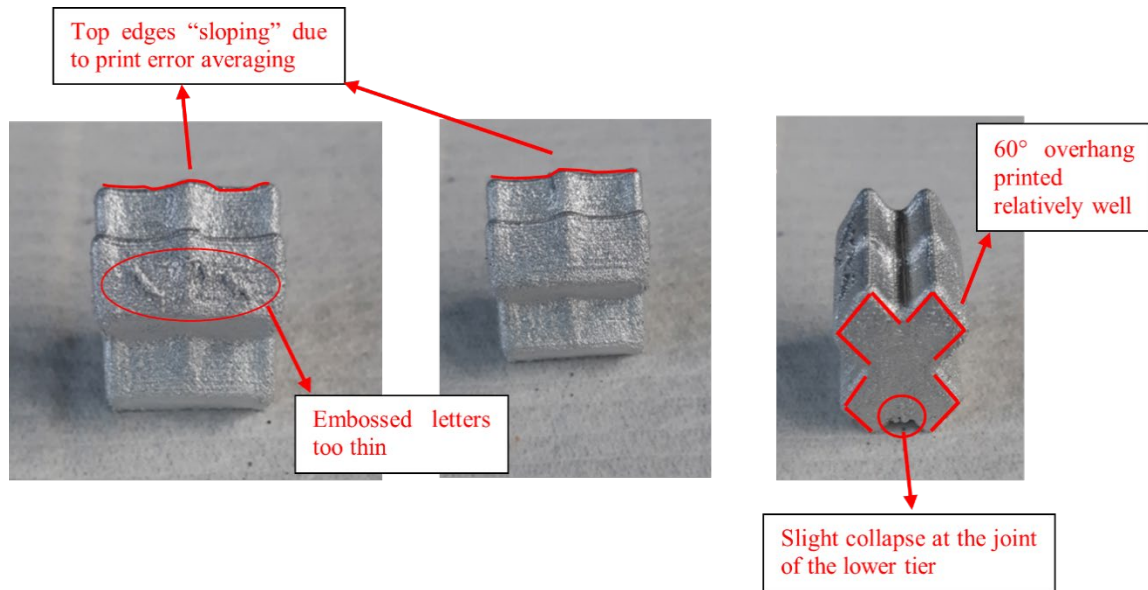
Figure 23. X-shaped part with paralellepiped voids

Observations for the Buoyant Model. This printed part took approximately 5 hours to complete. Overall, the wall thickness of 2 mm and the 60° overhang void structures were printed and managed to hold well to form the "X" shape. The shape and overhang of the parallelogram voids were more defined and did not collapse at the joint of the lower tier. This is because the rounded fillet (2 mm) seems to be within the design guidelines for unsupported structures. Since this part was printed with global correction (wide scan), the accumulated print errors were "averaged" throughout the print job, which resulted in the steep slope observed at the tip of the upper tier. This observed slope was due to the extensive print errors (either over/under mass deposition or sputtering), and averaging is required to compensate for those errors.

Furthermore, this printed part is not water-tight due to the porosities on the surface caused by either material lost due to splattering or because the accumulative print error is beyond the printer's ability to compensate. The features of the embossed letters were deliberately dimensioned to meet the printer's guidelines. However, the letter "P" turned out poorly due to its positioning (interface between the wall and sloping surface resulted in the disjoint). Refer to **Figure 24** for the pictorial description of the printed part.

Figure 24.   X-shaped (buoyant model) with paralepidid voids

Recommendation. To improve the print quality, the following adjustments were made to the printer's settings as well as to the subsequent models:

a.   **Where necessary, all sharp edges should maintain a fillet radius of 1–2 mm maximum, depending on the overhang angles. Higher overhang angles can afford a larger filet radius.**

b.   **The overhangs of 60° improved the uniformity of the printed void structure and prevented it from drooping downwards.**

c.   **Wall thickness shall be maintained at 2 mm since the wall features printed relatively well.**

d.   **In this prototype version of the Xerox LMP, the accumulated print error is further manifested as the print height increases, which is also why the print height was limited. Therefore, it is recommended to either orientate the print part such that the build height is minimum or to keep the desired build height as low as possible.**

3. [Results and Discussions] Double Parallelogram-Shaped Object with Parallelogram Voids

Printer Setting. This part was printed with **error diffusion settings**. The algorithm for Error diffusion programs the 3D printer to break the path of the print head into smaller processing segments to achieve better print resolution, i.e., sharper edges and well-defined features. In this mode, the part is not actively scanned to average out the errors; it works more like a tool-path optimizer ensuring accurate liquid metal deposition in the most optimized manner.

Observations. This printed part took approximately 2.5 hours to complete. The wall thickness of 2 mm was printed and managed to hold well. However, the shape and overhang of the parallelogram voids (at the joint) was observed to be less than 60°. Since this part was printed with error diffusion, the print errors at the beginning were not detected/ corrected, leading to the drooping overhang structure nearing the joint segment. Further accumulated print errors were manifested towards the end, which resulted in the surface porosity at the tip, and the structure was unable to "seal up." This printed part is not water-tight because of the porosities on the surface (between wall and void) caused by either material lost due to splattering, over/under deposition or because the accumulative print errors were not corrected/averaged. Thus, the printed voids could not "catch up" with the printed walls. Another stark feature of the printed part using error diffusion mode is the printer's ability to print well-defined features with sharp edges and smooth corners. This is made possible due to the tool-path optimizer ensuring accurate liquid deposition, and without the correction functions, there is no "averaging" or compensation which may lead to a sloping feature. The features of the embossed letters were printed relatively well. Refer to **Figure 25** for the pictorial description of the printed part.
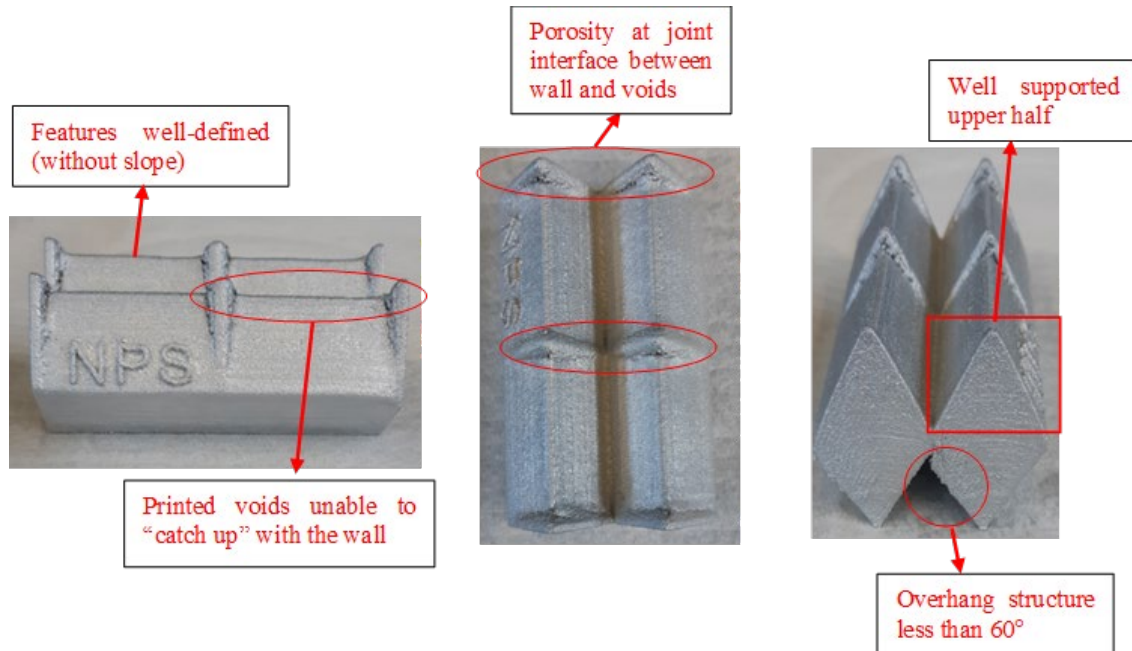
Figure 25.   Double parallelepiped with voids

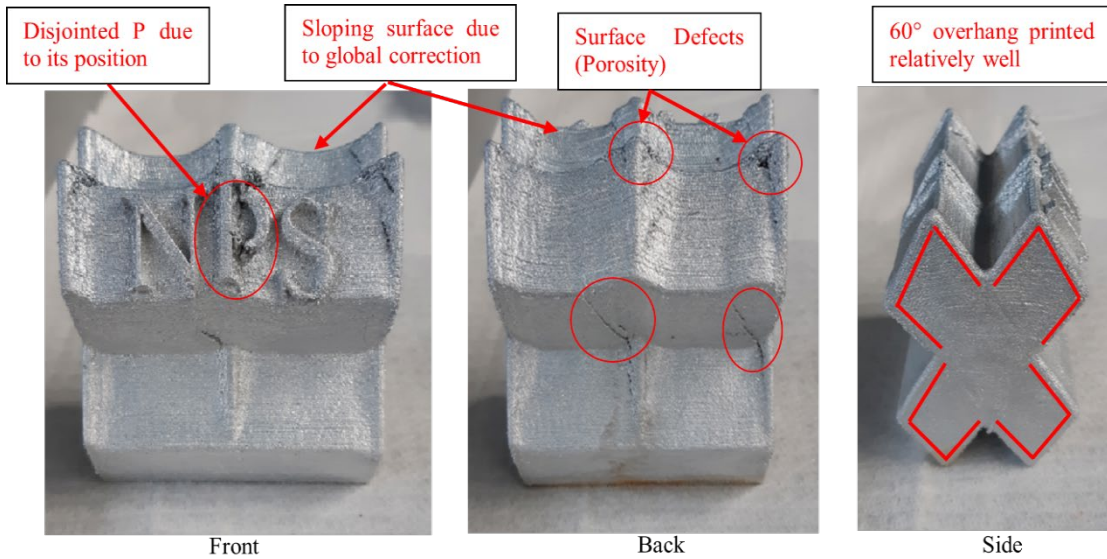Recommendation. To improve the print quality, the following adjustments were made to the printer's settings as well as to the subsequent models:

a. **Use error diffusion mode if features need to be well-defined. Print optimization will tend to cover up the errors and will result in features/ dimensions that are not of the specified tolerances (due to averaging out print errors).**

b. **Wall thickness will be increased to 3 mm to test whether the print features and overhang angles could print feasibly.**

c. **In this prototype version of the Xerox LMP, both error diffusion and print optimization were unable to accurately print structures with voids (even though printer guide was followed, i.e., overhang angles). To print internal voids, orientation and overhang angles of the void structures will need to be carefully considered to ensure the success of the printed part.**

4. [Results and Discussions] Cube-Shaped Model with Complex Internal Voids

Printer Setting. This part was printed with **error diffusion settings**. The reason for this setting selection (error diffusion) is to document and test whether the complex internal geometries can be printed to produce well-defined features using this mode. As highlighted before, the algorithm for Error diffusion programs the 3D printer to break the path of the print head into smaller processing segments to achieve better print resolution, i.e., sharper edges and well-defined features. In this mode, the part is not actively scanned to average out the errors; it works more like a tool-path optimizer ensuring accurate liquid metal deposition in the most optimized manner.

Observations. This printed part was deliberately stopped after completing 70% due to poor printed features and quality. It took approximately 6 hours to complete 70%. This print job is by far the longest because of the increased number of strokes due to the complex internal geometries. The wall thickness was adjusted to 3 mm and managed to print well for at least 30% before printing deteriorated subsequently (Refer to **Figure 26**). It was observed that the print job before the 30% mark was of a higher quality than the subsequent layers (Refer to **Figure 27**), and at around the 70% mark, the features of the internal geometries had collapsed. The main reason for this occurrence is because the metal jetting/ deposition seems to deteriorate as the print job progresses. After around four to five hours of printing, it was observed that the jetting quality drops (splattering/satellite droplets) and the mass deposition per unit time went out of calibration. Therefore, the pre-start and start procedures are critical (i.e., nozzle preparation, initial printer's set up and calibration) steps that will determine and maintain the print quality throughout the print job and even subsequent print jobs (printed within the same day). Deposition defects were also observed at the initial layers of the print job. This is likely caused by the splattering (inaccurate deposition) from the subsequent layers that fell onto the base of the interior features/voids (Refer to **Figure 27**).

Top layer after **30% print**	Top layer after **70% print**
Print quality started to deteriorate after 30%	Poor print quality and finishing observed after cumulative print errors

Figure 26.   Cube-shaped model with complex internal geometries (top layer)
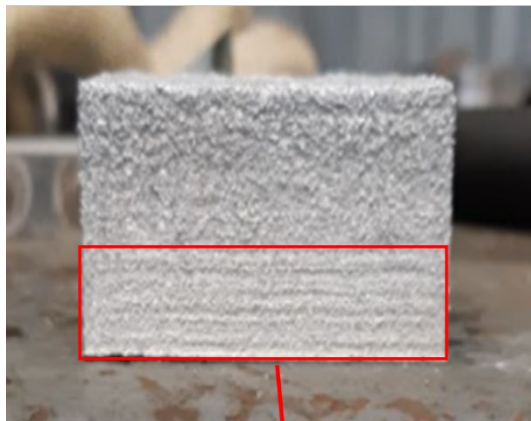
Bottom half (initial 30%) better print quality	Deposition defects at the bottom print layer
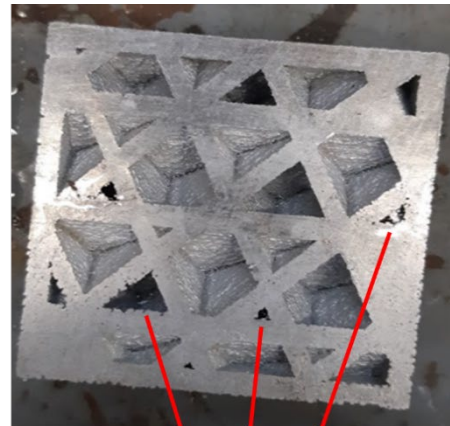
Figure 27.   Cube-shaped model with complex internal geometries (print quality and defects)

Recommendation. To improve the print quality, the following adjustments were made to the printer's settings as well as to the subsequent models:

a. **If the print quality/jetting was observed to have deteriorated (when printing is in progress), it is impossible to adjust or re-calibrate the printer mid-way into the job. The print job has to be stopped or completed before calibration can be conducted and subsequently to start a new print job. The (Xerox ElemX printer) improved or upgraded version should be designed such that it is able to pause the current print job, re-calibrate the printer, and resume the print job. In that case, it will help reduce material wastage and also improve the efficiency of part production.**

b. **The wall thickness shall be maintained at 3 mm before future upgrades to lower the tolerances for wall thickness.**

B. OBJECTIVE 2: FABRICATE LIGHTWEIGHT ENERGY ABSORBING STRUCTURES WITH THE INTENTION TO CONTROL DEFORMATION AND FAILURE MODES

3D Printed Test Specimen. To ensure sufficient samples for testing and data collection, five cylindrical test specimens were printed, each for the solid infill and the void infill samples.

1. [Results and Discussion] Compression Testing of Solid Infill

Solid Cylindrical Specimen (with solid infill). This test specimen was printed with error diffusion settings to achieve a consistent height across all five samples with a flat top and bottom to meet ASTM E9 test standards. The algorithm for Error diffusion programs the 3D printer to break the path of the print head into smaller processing segments to achieve better print resolution, i.e., sharper edges and well-defined features. **Figure 28** shows the five printed test specimens with solid infill.

Figure 28.   Solid cylindrical test specimen (solid infill)

Mechanical Properties. A total of three specimens with solid infills were tested and data collected to determine the mechanical properties. The stress-strain curve for the three specimens is shown in **Figure 29, 30 and 31**. The average values as presented in the summary table shown in **Table 3**.

Figure 29.　Stress-strain curve for specimen 1 (solid infill)

Figure 30.　Stress-strain curve for specimen 2 (solid infill)

Figure 31.   Stress-strain curve for specimen 3 (solid infill)

Table 3.   Summary of compression test data collected for solid infill.

Summary – Average for Test 1, 2 and 3				
Mass	Compressive yield Strength	Compressive Modulus	Toughness @ 16% Strain	Specific Energy Absorption
9.2 g	83 Mpa	6.6 Gpa	25.6 MJ/m³	**9974.7 J/Kg**

Deformation of Cylindrical Specimen. To quantify the amount of deformation experienced by the test specimen, the original diameter before compression was compared against the max diameter after compression (**Figure 32**). The original diameter was specified to be 13mm, and the average maximum diameter measured and recorded after the specimen underwent compressive deformation was **14.11mm**, as shown in **Table 4**.

Table 4.   Summary of maximum diameter recorded after compressive deformation.

Summary – Average for Test 1, 2 and 3				
	Test 1	Test 2	Test 3	Average
Max Diameter after Compression	14.14mm	14.17mm	14.04mm	**14.11mm**
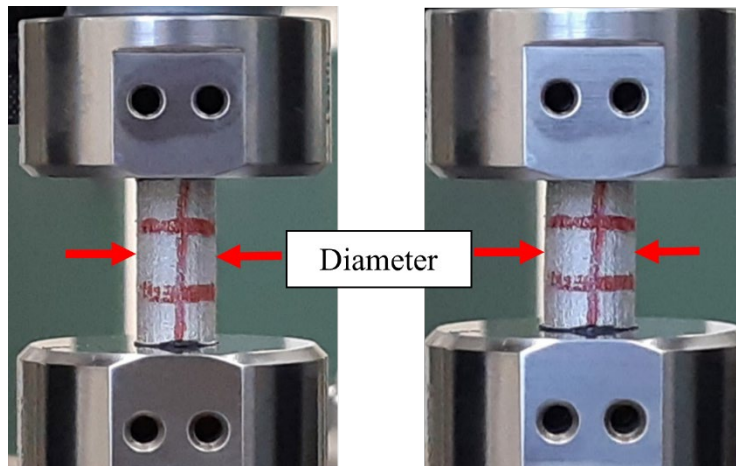
Figure 32.   Max diameter measured on the mid-section of specimen

2.   [Results and Discussion] Compression Testing of Void Infill

Solid Cylindrical Specimen (with void infill). This test specimen was printed with print optimization (global correction) settings to prevent protruding top (due to the void infills) and achieve a relatively flat top to meet ASTM E9 test standards. The algorithm for global correction programs the 3D printer to scan the printed part after every five layers to check on the features to determine if compensation is required so that reconfiguration of the droplet spacings and deposition can be adjusted to "average" out the print errors. While the top surface did not achieve the same level of flatness compared to the error diffusion, the global correction ensured that the protruding void is less defined and kept within the internal print volume. **Figure 33** shows the five printed test specimens with void infill.
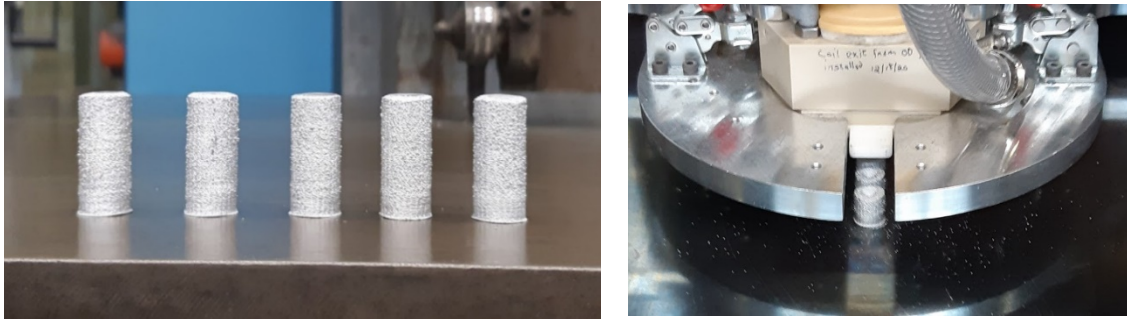
Figure 33.   Solid cylindrical test specimen (void infill)

Mechanical Properties. A total of three specimens with void infills were tested and data collected to determine the mechanical properties. The stress-strain curve for the three specimens is shown in **Figure 34, 35 and 36**. The average values as presented in the summary table shown in **Table 5**.
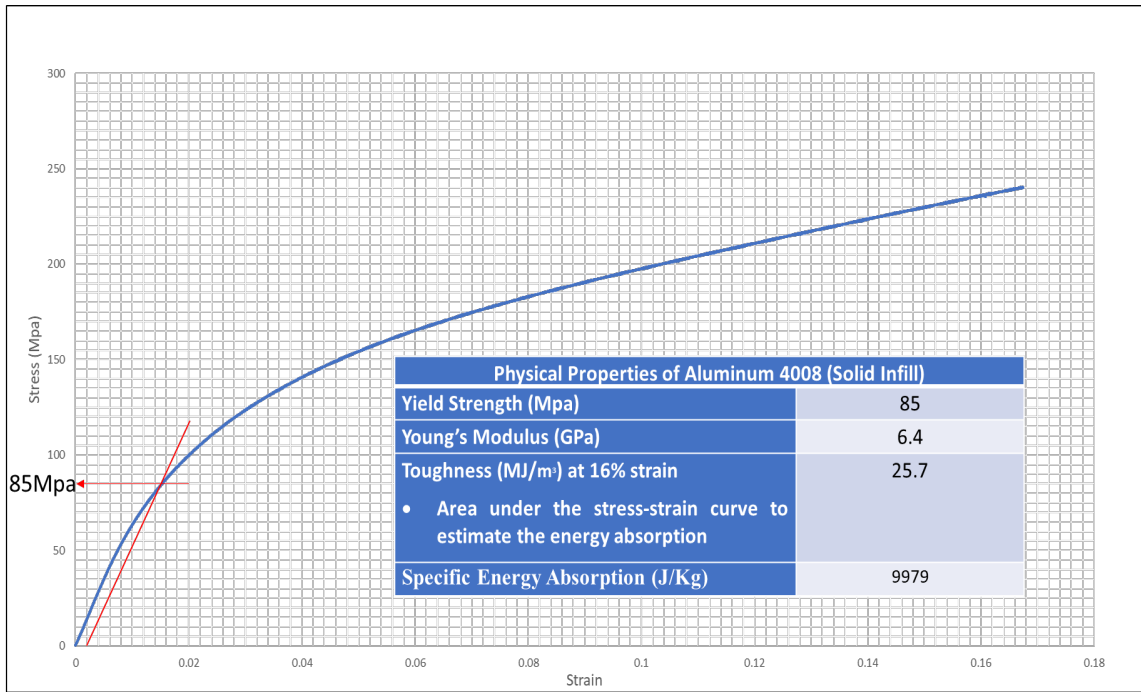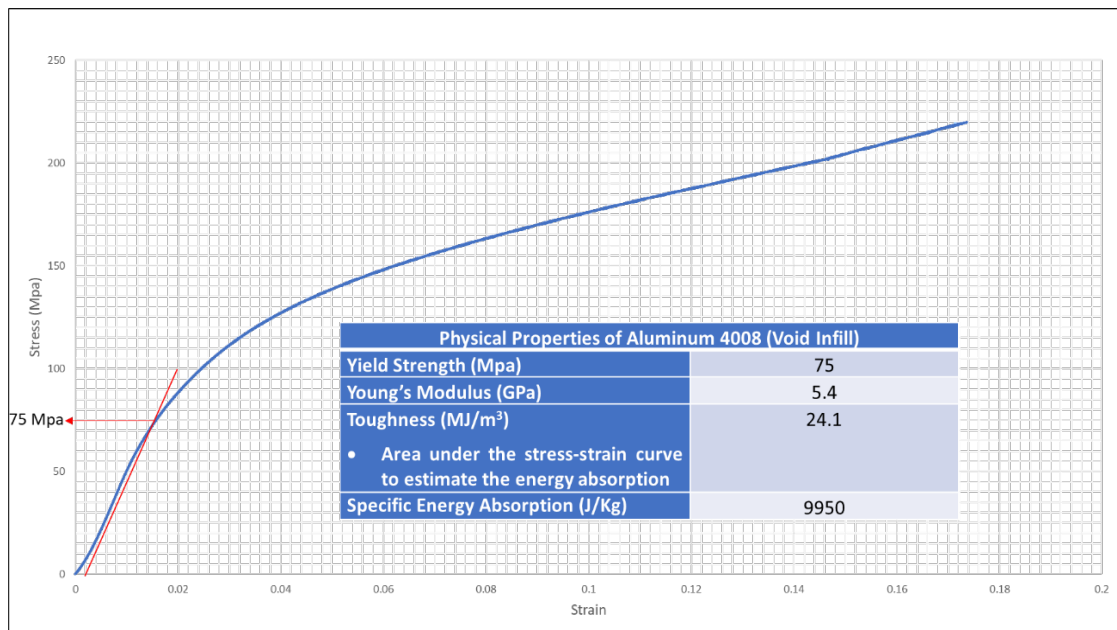

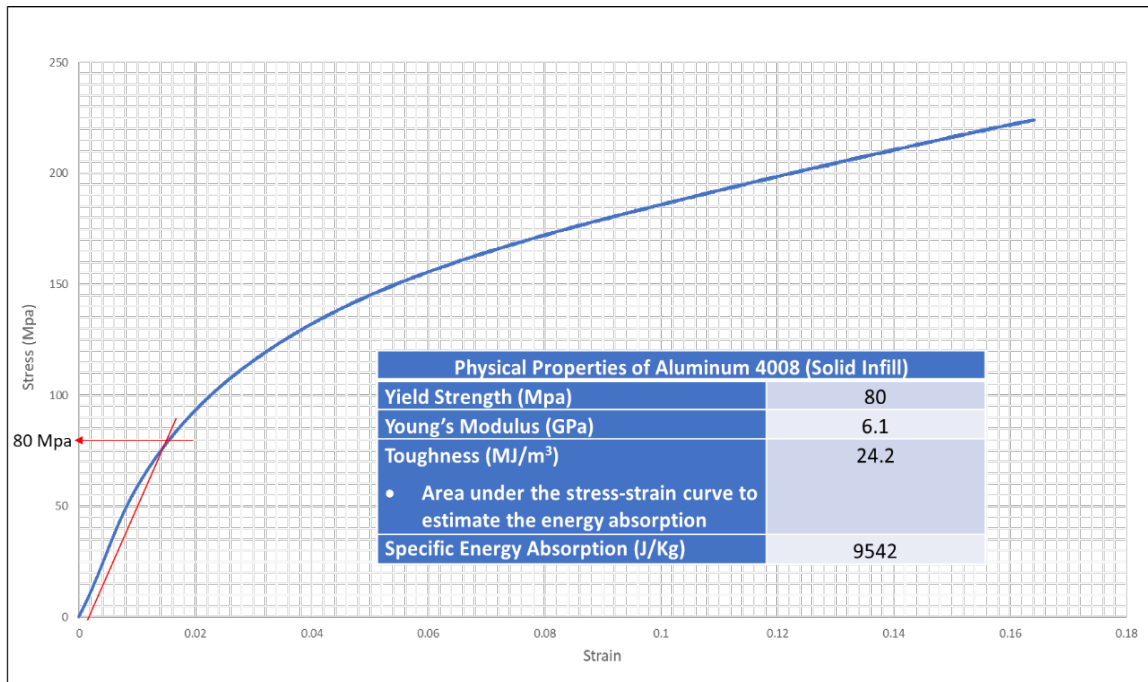Figure 34.   Stress-strain curve for specimen 1 (void infill)

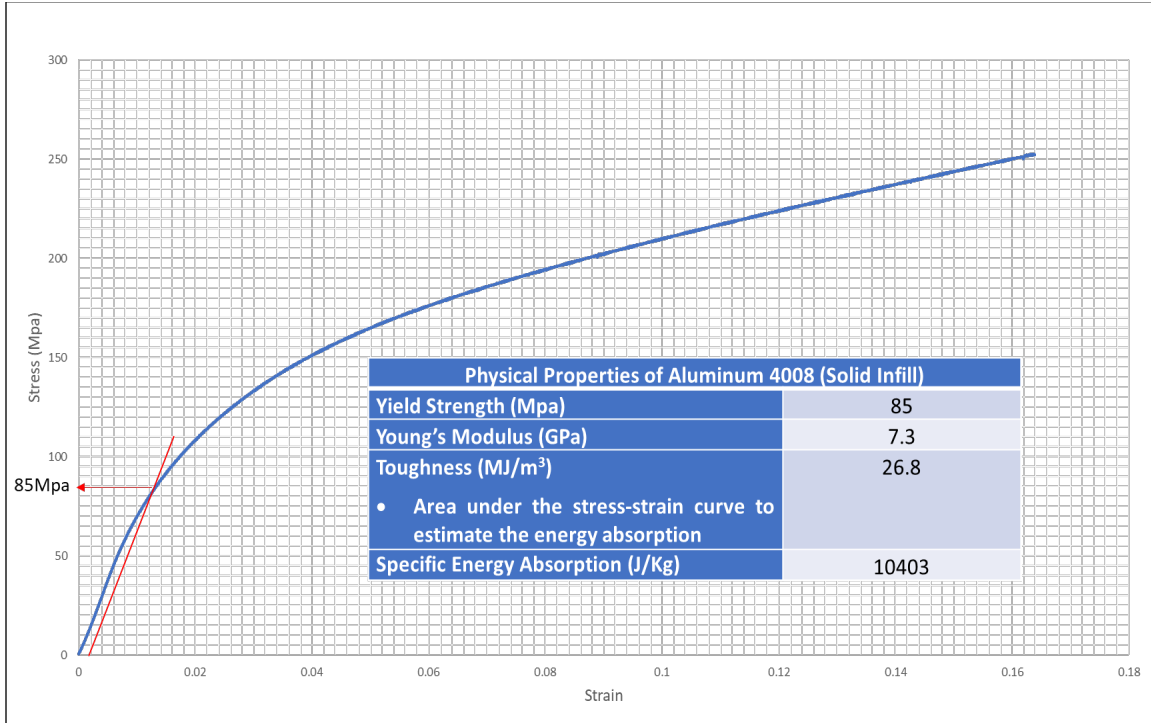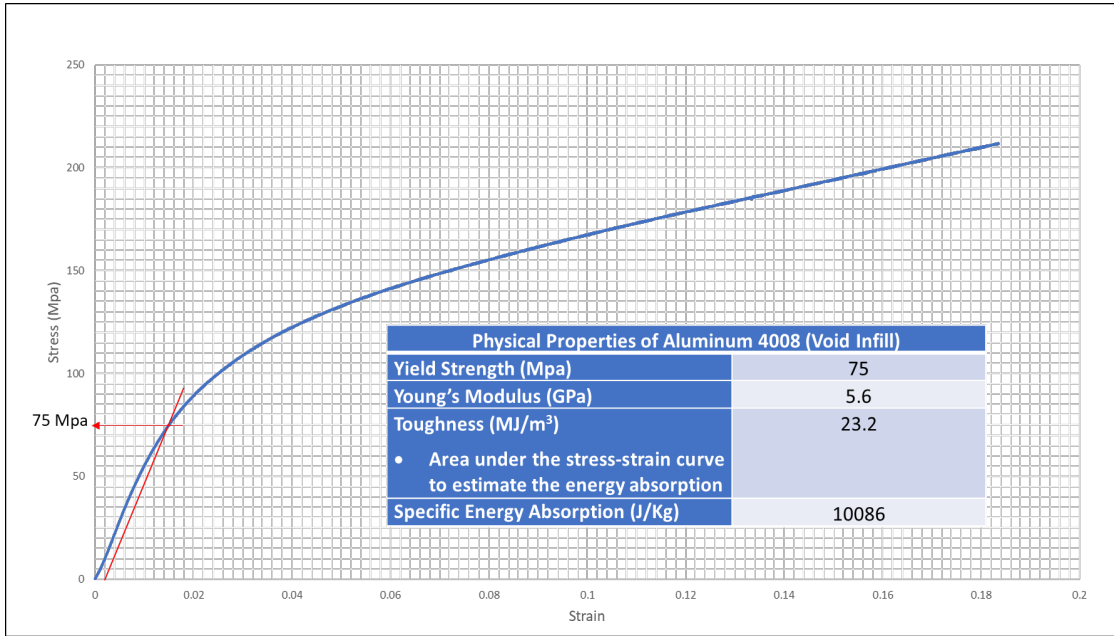Figure 35.   Stress-strain curve for specimen 2 (void infill)
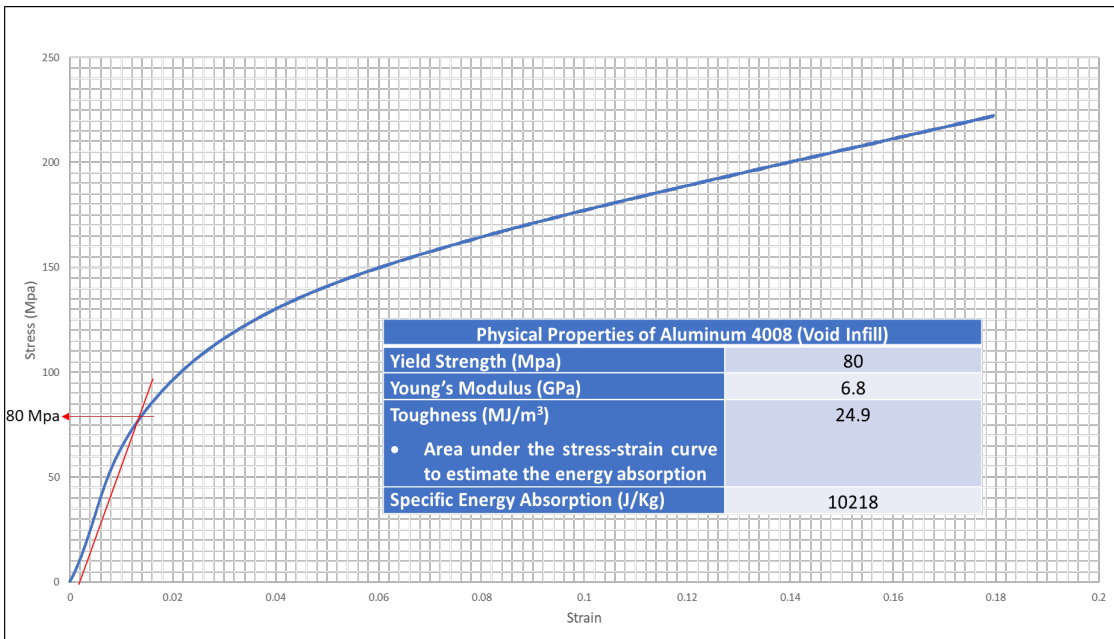
Figure 36.   Stress-strain curve for specimen 3 (void infill)

Table 5.　Summary of compression test data collected for void infill

Summary – Average for Test 1, 2 and 3				
Mass	Compressive yield Strength	Compressive Modulus	Toughness @ 16% Strain	Specific Energy Absorption
8.4 g	77 Mpa	5.9 Gpa	24 MJ/m^3	**10085 J/Kg**

Deformation of Cylindrical Specimen. The original diameter was specified to be 13mm, and the average maximum diameter measured and recorded after the specimen underwent compressive deformation was **14.92mm**, as shown in **Table 6**. As illustrated in **Figure 37**, the positioning of the internal void resulted in the controlled deformation and intended failure mode tailored to expand widest at the center of the specimen.

Table 6.　Summary of maximum diameter recorded after compressive deformation.

Summary – Average for Test 1, 2 and 3				
	Test 1	Test 2	Test 3	Average
Max Diameter after Compression	14.65mm	15.13mm	14.98mm	**14.92mm**
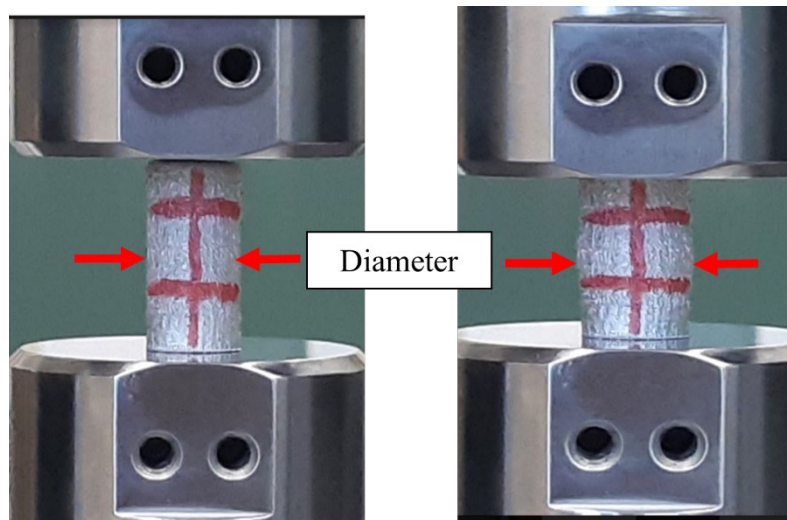
Figure 37.　Max diameter measured on the midsection of specimen

C. OBJECTIVE 3: DETERMINE THE EFFECTS OF THE AMBIENT/PRINT BED TEMPERATURE ON THE THERMAL STATE OF THE METAL DROPLET

1. [Numerical Analysis] Ambient Temperature Effects on the Thermal State of the Metal Droplet

To compute the thermal state of the metal droplet, the **lumped capacitance** and the **exact solution of one-dimensional transient heat conduction** methods will be utilized and compared. The ambient temperature will also be varied to test the effects it has on the thermal state of the metal droplet. Assuming quiescent air without forced convection, the thermal state of the metal droplet will be calculated from the time it is ejected from the print head and before it lands on the print bed; the flight distance is estimated to be 25 millimeters, and with an average flight velocity of 5m/s, the flight time of the droplet (assumed spherical shape with radius of 240μm) is estimated to be 5 milliseconds based on the ejection rate of the 3D printer. The following steps were taken to compute the analysis.

a. Determine Convective Heat Transfer Coefficient of Air (H_A).

The Biot number is a dimensionless ratio comparing the heat transfer resistance or conduction inside a body and convection at the surface of a body. The calculated Bi number of the metal droplet (0.0008) which is <<0.1 suggest that the temperature within the droplet is uniform as heat conduction within the droplet is faster than the heat convection away from the droplet at the surface. Furthermore, heat transfer by radiation is considered negligible due to its smaller magnitude when compared with Heat transfer by convection [26]. Thus, we need to determine the convective heat transfer coefficient of air (H_A) using the Ranz-Marshall Correlation first before applying it to subsequent equations. The Ranz-Marshall equation as shown in **Equation 1** [26]: where k_g: Gas thermal conductivity, Re: Reynolds number for flow, Pr: Prandtl Number, C_g: Gas heat capacity and C_g(avg): Gas heat capacity at the average temperate of the gas and droplet.

$$h = \frac{k_g}{d_d}(2.0 + 0.6\,\text{Re}^{1/2}\,\text{Pr}^{1/3})\left(\frac{C_{g(avg)}}{C_g}\right)^{0.26} \qquad (1)$$

The respective H_A for ambient temperature 50°C, 100°C, 150°C, 200°C was calculated using the Ranz-Marshall correlation and summarized in **Table 7**.

Table 7.   Summary of convective heat transfer coefficient of air (H_A)

Ambient Temperature	H_A (W/m².K)
50°C	476.72
100°C	490.28
150°C	503.35
200°C	515.80

b.   Determine Metal Droplet Temperature Profile through Lump Capacitance Method.

The lumped capacitance method is a suitable estimation of the metal droplet temperature given that the calculated Biot number of the metal droplet is 0.0008 which is significantly smaller than 0.1, suggesting that the droplet temperature can be treated as uniform throughout. The governing equation for Lumped analysis for Transient heat conduction is shown in **Equation 2** [27]: where T_f : Ambient temperature, T_o : Metal droplet initial temperature, t: Flight time, τ: Thermal time constant as shown in **Equation 3** [27], ρ: Density, C: Specific heat capacity, V/A: Characteristic length (r_0), and h: Convective heat transfer coefficient.

$$T(t) = T_f + (T_0 - T_f)e^{-t/\tau} \qquad (2)$$

$$\tau = \frac{\rho c \mathrm{V}}{hA} \qquad (3)$$

The ambient temperature effects on the metal droplet temperature profile were calculated and presented in **Figure 38**. Based on a flight time of 5 milli-second for each droplet, the temperature reduction (from 1098K – print head temperature) of the metal droplet for respective ambient temperature plot is between 2.5 and 3°C. Furthermore, the difference in ambient temperature has insignificant impact on the cooling of the metal droplet temperature (difference ranging between 0.5°C at 5ms).
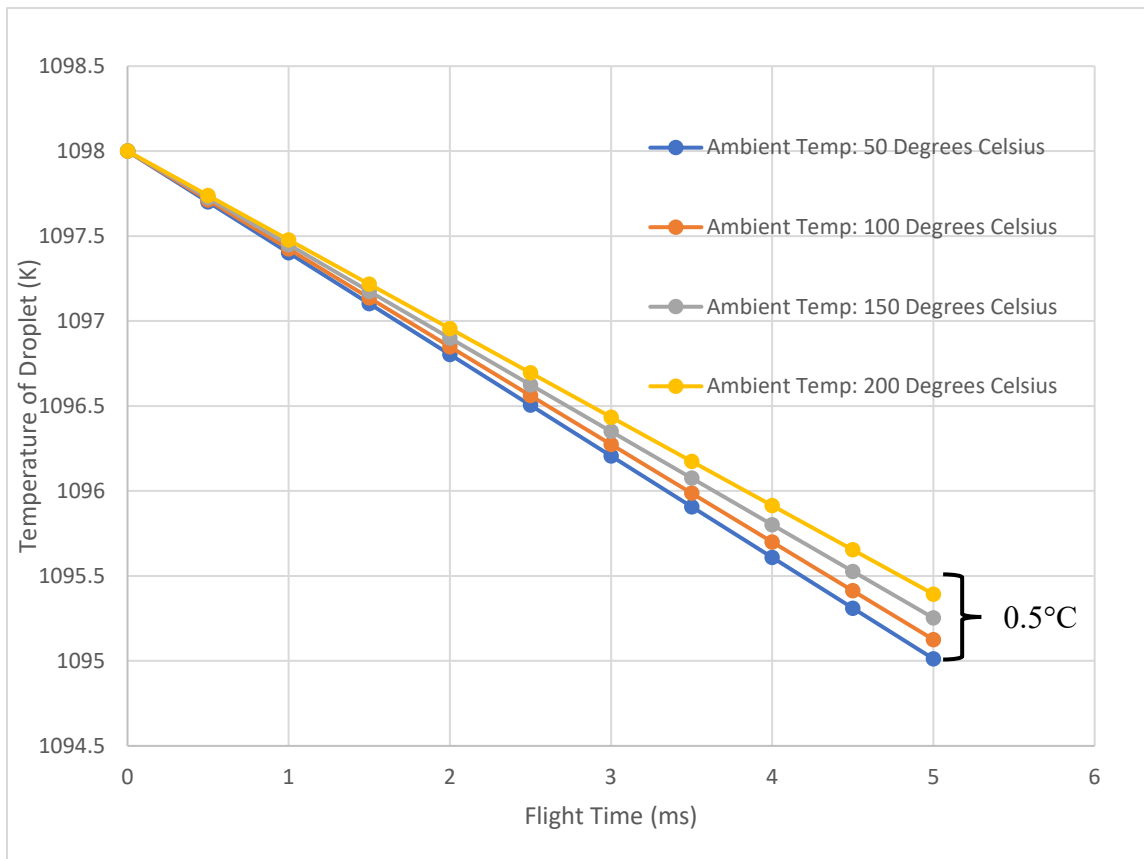
Figure 38.   Effects of ambient temperature on metal droplet during flight

c. Determine Metal Droplet Temperature Profile through approximate Solution for 1D Transient Heat Conduction.

The approximate solution for 1D transient heat conduction including spatial effects (i.e temperature gradient within metal droplet) was also calculated to compare with the lumped analysis method. The following **Equation 4** [28] was utilized: where λ_n: Roots of **Equation 5** [28], τ: Fourier number, x: Variable radius, and L: Radius of droplet.

$$\theta = \sum_{n=1}^{\infty} \frac{4(\sin \lambda_n - \lambda_n \cos \lambda_n)}{2\lambda_n - \sin(2\lambda_n)} e^{-\lambda_n^2 \tau} \frac{\sin(\lambda_n x/L)}{\lambda_n x/L} \qquad (4)$$

$$1 - \lambda_n \cot \lambda_n = \mathrm{Bi} \qquad (5)$$

The approximate solution accounting for spatial effects were computed and plotted as shown in **Figure 39** and **40**. **Figure 39** shows the effects of the ambient temperature on the metal droplet temperature profile calculated at a radius of 1μm (within the sphere). While **Figure 40** shows the metal droplet temperature profile calculated at a radius of 24μm (surface of sphere). Firstly, the temperature differences between the droplet at radius 1μm and 24μm is negligible, proving that we can neglect spatial effects, with uniform temperature within the droplet. Secondly, the impact of ambient temperature changes did not significantly alter the cooling rates or temperature profile of the metal droplet (difference of 0.2°C).
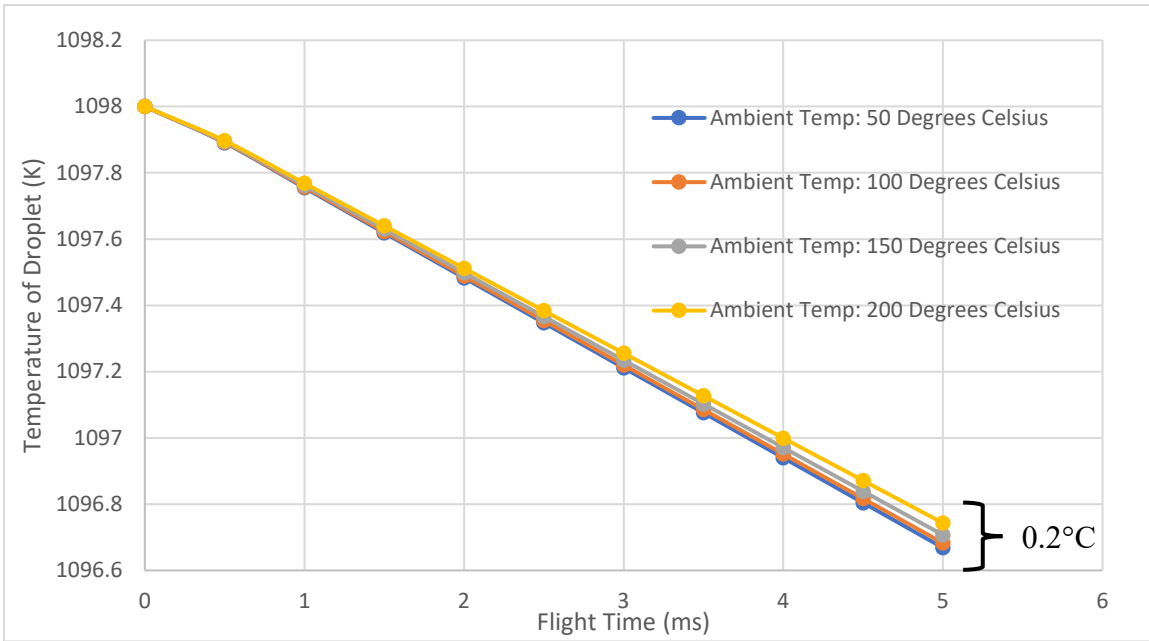
Figure 39.   Effects of ambient temperature on metal droplet @ radius 1μm during flight
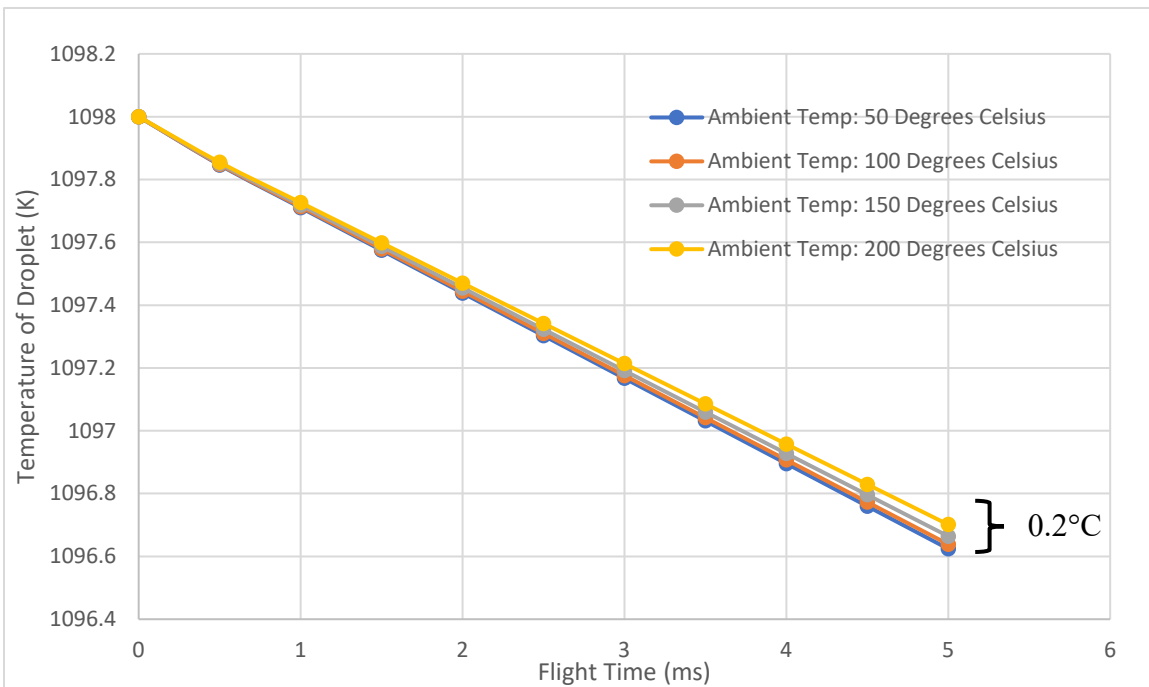
Figure 40.   Effects of ambient temperature on metal droplet @ radius 24μm during flight

2.   [Numerical Analysis] Print Bed and Substrate Temperature Effects on the Thermal State of the "Planar Splat"

Research have shown that temperature variation of base plate/substrate may affect the solidification of the droplet splat upon contact and therefore influence the splat's spread (maximum outreach, retraction, rebound), splat's defect (presence of trapped bubbles) and formation of solidified radial "ligaments" [29]. This numerical analysis will aim to showcase the impact of the print bed (Nickel plated brass) and aluminum substrate's temperature on the temperature profile of the planar splat upon contact.

Assumptions. Heat loss through convection and radiation after the droplet contact with the base plate is considered negligible due to the relatively short time it takes before solidification. The heat conduction and energy conservation equations will be used to compute the interface temperature between the splat and substrate (**Figure 41**).
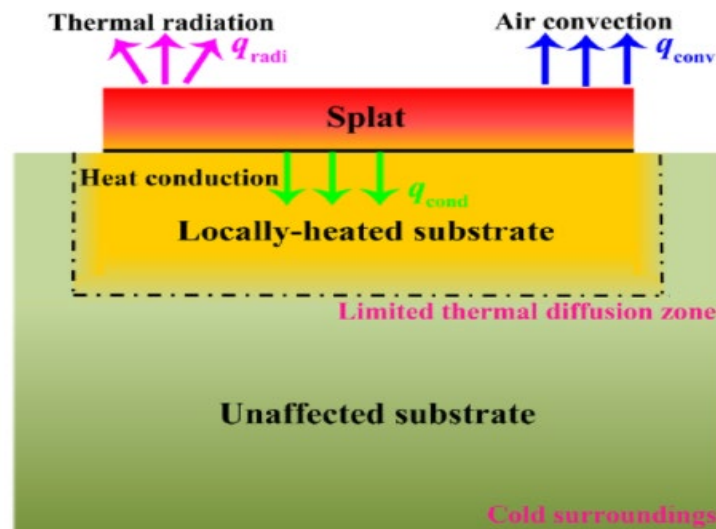
Figure 41.   Illustration of the splat's heat interaction with the substrate.
Source: [30].

The interface temperature of the splat was calculated using the following heat conduction and energy conversation **Equations 6, 7, 8** [30]: where D: Thermal diffusivity of baseplate/substrate, t: Time, T_d: Temperature of substrate, T_m: Melting temperature of Droplet, T_i: Interface temperature between splat and substrate, ρ_l: Density of droplet, ρ_s: Density of substrate, C_{pl}: Specific heat capacity of metal droplet, C_{ps}: Specific heat capacity of substrate, δ: Thickness of splat. Therefore, **equation 8** expresses the interface temperature at T(0,t).

$$T(x,t) - T_d = \frac{\Lambda_0}{\sqrt{\pi Dt/8}} e^{-2x^2/Dt} \qquad (6)$$

$$\Lambda_0 = \frac{\rho_1 C_{pl}}{\rho_s C_{ps}} \delta(T_m - T_i) \qquad (7)$$

$$T(0,t) = \frac{\frac{\rho_1 C_{pl}}{\rho_s C_{ps}} \delta T_m + \sqrt{\pi Dt/8} T_d}{\frac{\rho_1 C_{pl}}{\rho_s C_{ps}} \delta + \sqrt{\pi Dt/8}} \qquad (8)$$

After the initial metal droplet contacted the print bed (base plate), the temperature profile and cooling rates of the splat varies with the print bed temperature (648K, 748K and 848K) as shown in **Figure 42**.

Print Bed Temperature of 848K. With a higher print bed temperature, which is closer to the droplet temperature, the splat's temperature will remain above the liquidus line beyond 8000μs. This may result in the rebound of the splat as it did not solidify after coming into contact with the print bed [29]. This rebound is undesirable because material is lost during deposition, and the 3D printed part would not build to specification.

Print Bed Temperature of 748K. This temperature setting is currently the default setting of the XeroX ElemX printer. The splat's "mushy zone" is between 1540μs and 6930μs, suggesting that the splat would most likely solidify at the bottom layer first and remain mushy towards the top during this period. This partially solidified splat would then be the "window of opportunity" to facilitate subsequent droplets with varying frequency and ejection speed (depending on program algorithms) to better adhere and form bonds to maximize material properties. This is because, droplet coalescence will be best achieved when the temperature at the top/tip of the splat is at the melting point of the metal [31]. For example, the Xerox ElemX 3D printer prints the infill at 400Hz, and assuming the droplet speed of 5m/s, the time separation between droplets is 2500μs, which is well within the mushy zone's time span of the previous splat.

Print Bed Temperature of 648K. With a larger temperature delta from the droplet temperature, the splat will cool down and solidify significantly faster. The splat's "mushy zone" is between 520 - 1430μs. The "window of opportunity" at which the splat remains partially mushy is short with expected rapid solidification. Subsequent droplets that are deposited on fully or almost fully solidified splat may not bond or coalesce strongly, leading to undesirable gaps within the 3D printed parts with degraded material properties. Due to the cooler substrate, the higher cooling rates experienced by the deposited droplets will cause the lack of strong bonding with subsequent deposited droplets [32].

Thus, careful consideration is required to choose a print bed with sufficient protection against high temperature oxide formation and suitable thermal conductivity to control the splat's thermal cooling rates. From the numerical analysis shown in **Figure 42**, it is critical to identify and select the optimum print bed temperature required to facilitate the desired cooling and solidification rate of the splat upon contact.

51
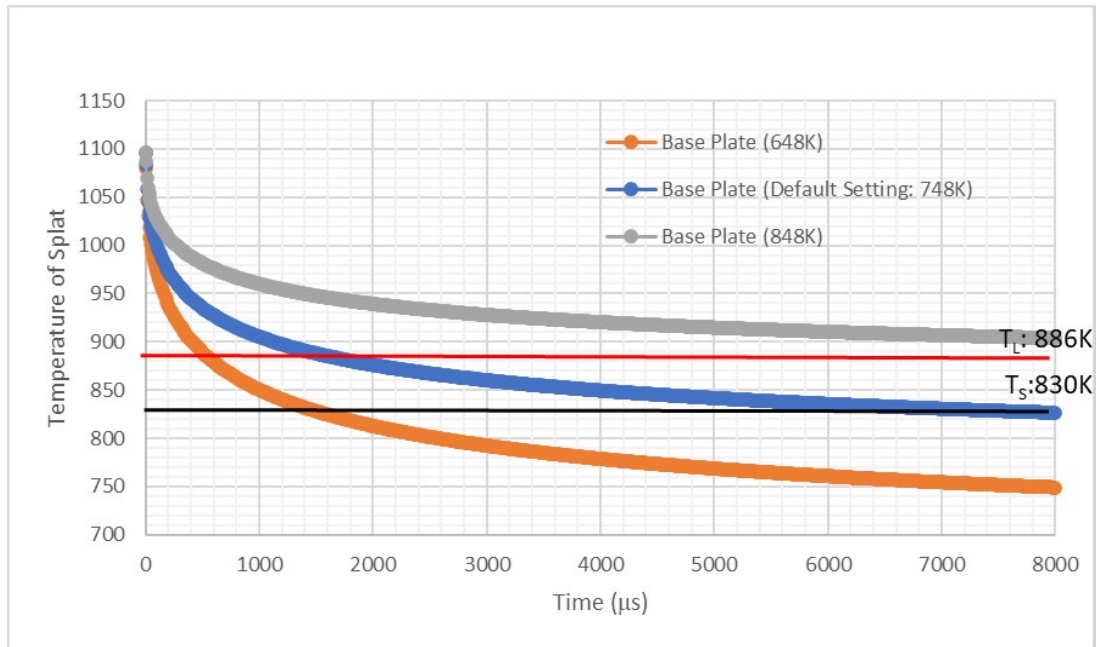
Figure 42.   Temperature profile of splat (after contact with print bed)

The bulk of the metal droplets will come in contact with the aluminum substrate subsequently once the initial layering has completely bonded with the base plate. Therefore, the temperature profile of the splat will be derived based on the interaction between the aluminum substrate and aluminum metal droplet as illustrated in **Figure 43**. For substrate temperature of 848K, the splat's temperature profile remains above the liquidus line during the initial 8000μs. For the default setting temperature of 748K, the splat's "mushy zone" is between 1420 and 6370μs. As for the substrate temperature of 648K, the splat's "mushy zone" is between 480 and 1310μs. In contrast with the print bed, the aluminum substrate model yielded earlier occurrence of the "mushy zone" and shorter time span during the "mushy zones." This also meant that the frequency and speed of the droplet would need to be adjusted slightly upwards to keep up with the window of opportunity.
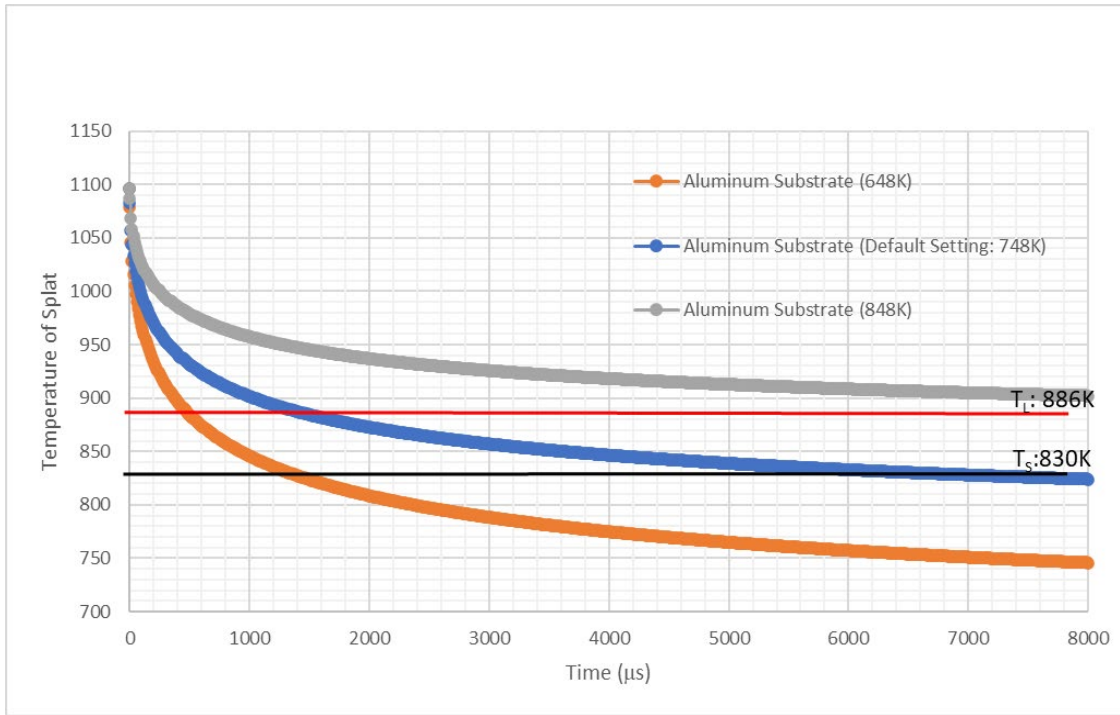
Figure 43.   Temperature profile of splat (after contact with aluminum substrate)

THIS PAGE INTENTIONALLY LEFT BLANK

IV.   CONCLUSIONS

This thesis paper set out with three objectives to analyze, demonstrate and test the 3D printer's capability to produce parts that are suitable for marine application; (1) To **build low-density water-tight buoyant structures** with **internal cavities**, (2) To **fabricate lightweight energy-absorbing structures** with the intention to **control deformation and failure modes**, and (3) Investigate the **effects of the ambient and print bed/substrate temperature** on the **thermal state of the metal droplet**.

Building Low-Density Water-Tight Buoyant Structures. Despite following the printer's guidelines, adjusting the printer settings, and fine-tuning the CAD models, the current version (1.0) of the Xerox LMP was unable to accurately print structures with overhangs (higher angled overhangs have better success rate) and internal cavities. This conclusion was evident from the observed outcomes of the printed buoyant structures. However, through this process, key insights into the printer's capabilities were gleaned;

   **a.**   **Accumulated print error is further manifested as the print height increases, which is also why the print height for the current version was limited. Therefore, it is recommended to either orientate the print part such that the build height is minimum or to keep the desired build height as low as possible.**

    b.   **All sharp edges should be filleted and rounded to prevent the printer head from taking a sharp turn while turning corners. A rounded corner will facilitate a smoother transition from the X to Y-axis and vice versa. Furthermore, it should reduce print time and improve the part printing efficiencies.**

    c.   **Depending on the overhang angles, it is still essential to maintain a fillet radius of 1–2mm maximum on the sharp edges of the overhang. Higher overhang angles can afford a larger filet radius.**

    d.   **Use Error diffusion mode if printed features need to be accurate and well-defined. This mode is most effective when print errors such as sputtering/satellite deposition and over/under mass deposition is minimized and kept within calibrated tolerances.**

    e.   **Use Print optimization mode if an approximate model is required. This mode will tend to cover up the errors and result in features/dimensions**

that are not of the specified tolerances (due to averaging out print errors). This mode could do correction and accommodate some amount of print errors. Note: This mode will take slightly longer to print because part scanning is required after every five printed layers.

f.   Both error diffusion and print optimization were unable to accurately print structures with voids (even though printer guide was followed, i.e., overhang angles). To print internal voids, orientation and overhang angles of the void structures will need to be carefully considered to ensure the success of the printed part.

g.   If the print quality/jetting was observed to have deteriorated (when printing is in progress), it is impossible to adjust or re-calibrate the printer mid-way into the job. The print job has to be stopped or completed before calibration can be conducted and subsequently to start a new print job. Suppose the (Xerox ElemX printer) future upgrade or improved version could pause the current print job, re-calibrate the printer, and resume the print job. In that case, it will help reduce material wastage and also improve the efficiency of part production.

h.   The wall thickness shall be maintained at 3mm before future upgrades to lower the tolerances for wall thickness.

Energy Absorbing Structures. The specific energy absorption for both the solid infill and void infill was measured to be **9974.7J/Kg** and **10084J/Kg,** respectively. The cone-shaped void infill specimen had recorded a slightly higher specific energy absorption due to its lighter weight and well-structured internal cell, which is capable of load-bearing.

Controllable Deformation. Ensuring the safety and water-tight integrity of ships and unmanned vessels will continue to be of paramount importance to mariners. Therefore, **tailoring the failure mode of water-tight load/impact bearing structures** ensures that deformation caused by impact or shock can **be predicted and contained without catastrophic consequences**. The simple proof of concept presented in this term paper has shown that the internal voids' strategic placement had resulted in the intended maximum deformation to occur in the specimen's center. The normal solid infill specimen had a more uniform deformation and a max diameter of 14.11mm in the center. In contrast, the void infill specimen had the deformation concentrated in the center and measuring a **max diameter of 14.92mm** under the same compressive loads and strain.

Numerical Analysis of the Metal Droplet Thermal State. It was concluded that the ambient temperature has insignificant impact on the thermal state of the metal droplet during flight time. Upon contact with the base plate/aluminum substrate, the splat would most likely solidify at the bottom layer first and remain mushy towards the top. This partially solidified splat would then be the "window of opportunity" to support good adhesion for subsequent splats. Therefore, the type of material used for the base plate and the selection of base plate/substrate temperature will directly impact the thermal state of the splat and affect the mechanical properties of the 3D-printed part.

Thus, all three objectives for the thesis work were fulfilled, proven by simply designed objects printed by the Xerox ElemX 3D Printer, and the conduct of numerical analysis utilizing heat transfer modelling and equations.

THIS PAGE INTENTIONALLY LEFT BLANK

V.   FUTURE WORK

Xerox ElemX Version Upgrade. The Xerox ElemX Liquid metal 3D printer was tested and trialled to print parts suitable for marine applications. To improve the print quality of overhang structures and internal voids, future ElemX upgrades should be considered for both hardware and software.

a.   **Hardware. Jetting quality and mass deposition are dependent on the user's performance in carrying out the pre-start and start procedures. Since this is manually conducted, different users with a lack of experience may not be able to consistently re-create an adequately prepared nozzle, for example, and cause subsequent inconsistencies in the quality of the printed part. Thus, if these processes (nozzle preparation, drop mass calibration, for example) can be automated, it will eliminate print errors introduced by the users.**

b.   **Software. The print settings such as the global correction and error diffusion will result in different outcomes depending on the user's requirements. However, software control over the amount of metal deposited and the frequency range at which it is deposited to create the desired shape will also determine the quality of the printed parts. Data could be collected from all printed jobs to collate information for a "range" of frequency that is feasible to print different shapes and sizes as well as for the infills or perimeter of the part. Data collected could then be used to determine a combination of jetting frequencies to accomplished complex features with a high probability of success.**

c.   **Thin Wall features. The current guide for wall thickness is relatively large, considering the good print accuracy. It was proven in this research that a wall thickness of 1mm could be printed, and future software should also be upgraded to support the printing of thin walls.**

d.   **Heat distribution and Temperature on Printed Part. Currently, heat is transmitted to the printed part via the print bed, and it is successful in maintaining a uniform temperature throughout the printed part. However, suppose the build height restriction is removed. In that case, the temperature of parts at higher heights may not have a uniform temperature (too far from the print bed), therefore the need to consider**

having heating elements to ensure uniform temperature throughout the printed part.

Energy Absorbing Structures for Marine Applications. We examined the various unit cells and stacking pattern that could form a limitless combination of energy-absorbing structures. Unit cells of other geometries, dimensions and varying gradient may be tested in the form of a lattice, honeycomb or foam structure to determine which cell pattern and arrangement are well suited for energy-absorbing structures. A suitable pattern that is tested could then be selected for marine applications such as a ship's berthing fender (for cushioning) and even hull protection for unmanned or coastal vessels.

Physical Observation of Metal Droplet/Splat. We could examine the physical state of the splat at different print bed/substrate temperature and determine the ideal ejection speed and frequency to support good adhesion and bonding of splats with minimum defects such as gaps or material lost due to rebound. Adjustments to the print bed/substrate temperature could also be made to achieve the desired thermal cooling rates of the planar splats.

LIST OF REFERENCES

[1]   GMTT Team, "Global marine technology trends 2030," Lloyd's Register, QinetiQ and University of Southampton, UK, Aug. 2015. [Online]. Available: https://www.lr.org/en-us/insights/global-marine-trends-2030/global-marine-technology-trends-2030/

[2]   F. Koh, "More piracy cases in Singapore Strait so far this year than in whole of 2019," *The Straits Times*, Nov. 23, 2020. [Online]. Available: https://www.straitstimes.com/singapore/more-piracy-cases-in-singapore-strait-so-far-this-year-than-in-whole-of-2019

[3]   M. Z. Lim, "Refurbished patrol vessels part of new navy flotilla," *The Straits Times*, Jan. 27, 2021. [Online]. Available: https://www.straitstimes.com/singapore/refurbished-patrol-vessels-part-of-new-navy-flotilla

[4]   B. Werner, "CNO Gilday releases new, simplified command guidance to fleet," *USNI News*, Dec. 04, 2019, p. 7. [Online]. Available: https://news.usni.org/2019/12/04/cno-gilday-releases-new-simplified-command-guidance-to-fleet

[5]   National Research Council, Division on Engineering and Physical Sciences, National Materials and Manufacturing Board, and Committee on Benchmarking the Technology and Application of Light-weighting, *Application of Light-weighting Technology to Military Aircraft, Vessels, and Vehicles*. Washington, DC, USA: National Academies Press, 2012, pp. 61–84.

[6]   J. Newman, "3D printed boats may be the future of the Royal Navy," *Digital Engineering*, Sep. 08, 2015. [Online]. Available: https://www.digitalengineering247.com/article/3d-printed-boats-may-be-the-future-of-the-royal-navy

[7]   G. Kardys, "Factors to consider when 3D printing or additive manufacturing metal parts," *Engineering 360*, Dec. 19, 2017. [Online]. Available: https://insights.globalspec.com/article/7447/factors-to-consider-when-3d-printing-or-additive-manufacturing-metal-parts

[8]   T. Alsop, "Most used 3D printing technologies 2020," *Statista*, Jun. 03, 2020. [Online]. Available: https://www.statista.com/statistics/560304/worldwide-survey-3d-printing-top-technologies/

[9]   E. Maslin, "Unmanned marine systems, squared," *Offshore Engineer Magazine*, Nov. 09, 2020. [Online]. Available: https://www.oedigital.com/news/483059-unmanned-marine-systems-squared

[10]   Ogle Models, "Unmanned surface vessel | Ogle Models & Prototypes Ltd," Dec. 21, 2017. [Online]. Available: https://www.oglemodels.com/case-studies/unmanned-surface-vessel/

[11]   Rushabh Haria, "Royal Navy unveils 3D printed 'Nautilus 100' mothership concept," *3D Printing Industry*, Sep. 02, 2017. [Online]. Available: https://3dprintingindustry.com/news/royal-navy-unveils-3d-printed-nautilus-100-mothership-concept-120783/

[12]   L. Gibson and M. F. Ashby, *Cellular Solids: Structure and Properties*, Second Edition. UK: Cambridge University Press, 1997, pp. 2–30.

[13]   C. Pan, Y. Han and J. Lu, "Design and optimization of lattice structures: A review," *Applied Sciences*, vol. 10, no. 18, p. 3, Sep. 2020. [Online]. doi: 10.3390/app10186374

[14]   M. Brandt, *Laser additive manufacturing*. Amsterdam, Netherlands: Elsevier, 2017, pp. 31–32.

[15]   O. Al-Ketan, R. Rowshan and R. Abu Al-Rub, "Topology-mechanical property relationship of 3D printed strut, skeletal, and sheet based periodic metallic cellular materials," *Additive Manufacturing*, vol. 19, pp. 167–183, Jan. 2018. [Online]. doi: 10.1016/j.addma.2017.12.006

[16]   Y. Xie and X. Chen, "Support-free interior carving for 3D printing," *Visual Informatics*, vol. 1, no. 1, pp. 9–15, Mar. 2017. [Online]. doi: 10.1016/j.visinf.2017.01.002

[17]   J. Banhart, "What are cellular metals and metal foams?" *Cellular Metallic Material*. [Online]. Available: http://www.metalfoam.net/

[18]   J. Banhart, "Metal foams – From fundamental research to applications," Frontiers in the Design of Materials, India: Universities Press (India) Limited, 2005.

[19]   Z. Zhang, H. Lei, M. Xu, J. Hua, C. Li and D. Fang, "Out-of-plane compressive performance and energy absorption of multi-layer graded sinusoidal corrugated sandwich panels," *Materials & Design*, vol. 178, p. 2, Sep. 2019. [Online]. doi: 10.1016/j.matdes.2019.107858

[20]   L. Griffiths, "Xerox acquires liquid metal 3D printing company Vader systems," *TCT Magazine*, Feb. 08, 2019. [Online]. Available: https://www.tctmagazine.com/additive-manufacturing-3d-printing-news/xerox-acquires-metal-3d-printing-vader-systems/

[21]   Xerox, "Additive Manufacturing Innovation with 3D Printing," Nov. 18, 2019. [Online]. Available: https://www.xerox.com/en-us/innovation/insights/additive-manufacturing-3d-printing

[22]   Instron.us, "What is compression testing?." [Online]. Available: https://www.instron.us/en-us/our-company/library/test-types/compression-test

[23]   Xerox, "Xerox ElemX Operating Instruction Manual Version 1.0," unpublished.

[24]   Xerox, "Xerox ElemX Design Guide and Machine Specification Version 1.0," unpublished.

[25]   Standard Test Methods of Compression Testing of Metallic Materials at Room Temperature, ASTM E9-19, ASTM International, 2019. [Online]. doi: 10.1520/E0009-19

[26]   J.-P. J. Cherng, "Solidification and cooling analysis of aluminum alloy droplets with the uniform droplet spray process," M.S. thesis, Dept. of Mechanical Engineering, Massachusetts Institute of Technology, Cambridge, MA, USA, pp. 27–28, 1997. [Online]. Available: https://core.ac.uk/download/pdf/4408227.pdf

[27]   M. Mahmoud, *Engineering Thermofluids: Thermodynamics, Fluid Mechanics and Heat Transfer*. Berlin, Germany: Springer, 2005, pp. 445–447.

[28]   J. H. VanSant, "Conduction heat transfer solutions," Lawrence Livermore National Lab. (LLNL), Livermore, CA, USA, Rep. UCRL-52863, p. 324, Mar. 1980. [Online]. Available: https://www.osti.gov/servlets/purl/6224569

[29]   M. V. Gielen, Rielle de Ruiter, R. B. J. Koldeweij, D. Lohse, J. H. Snoeijer, and H. Gelderblom, "Solidification of liquid metal drops during impact," *J. Fluid Mech.*, vol. 883, Oct. 2019. [Online]. doi: 10.1017/jfm.2019.886

[30]   L. Chen and G. Yang, "Epitaxial growth and cracking mechanisms of thermally sprayed ceramic splats," *J. Therm. Spray Tech*, vol. 27, no. 3, pp. 264–265, Feb. 2018. [Online]. doi: 10.1007/s11666-018-0692-4

[31]   M. Fang, S. Chandra, and C. B. Park, "Experiments on Remelting and Solidification of Molten Metal Droplets Deposited in Vertical Columns," *Journal of Manufacturing Science and Engineering*, vol. 129, no. 2, pp. 311–318, Sep. 2006. [Online]. doi: 10.1115/1.2540630

[32]   FLOW-3D, "Liquid Metal 3D Printing | Additive Manufacturing," [Online]. Available: https://www.flow3d.com/products/flow3d-am/liquid-metal-3d-printing/

THIS PAGE INTENTIONALLY LEFT BLANK

INITIAL DISTRIBUTION LIST

1.   Defense Technical Information Center
        Ft. Belvoir, Virginia

2.   Dudley Knox Library
        Naval Postgraduate School
        Monterey, California